Effects of matrix viscoelasticity on the lateral migration of a deformable drop in a wall-bounded shear

Swarnajay Mukherjee[1] and Kausik Sarkar[2],†

[1]Department of Mechanical Engineering, University of Delaware, Newark, DE 19716, USA

[2]Department of Mechanical and Aerospace Engineering, George Washington University, Washington, DC 20052, USA

The dynamics of a drop deforming, orienting and moving in a shear flow of a viscoelastic liquid near a wall is numerically investigated using a front-tracking finite-difference method and a semi-analytic theory. The viscoelasticity is modelled using the modified FENE-CR constitutive equation. In a Newtonian system, deformation in a drop breaks the reversal symmetry of the system resulting in a migration away from the wall. This study shows that the matrix elasticity reduces the migration velocity, the reduction scaling approximately linearly with viscoelasticity (product of the Deborah number *De* and the ratio of polymer viscosity to total viscosity β). Similar to a Newtonian system, for small Deborah numbers, the dynamics quickly reaches a quasi-steady state where deformation, inclination, as well as migration and slip velocities become independent of the initial drop–wall separation. They all approximately scale inversely with the square of the instantaneous separation except for deformation which scales inversely with the cube of separation. The deformation shows a non-monotonic variation with increasing viscoelasticity similar to the case of a drop in an unbounded shear and is found to influence little the change in migration. Two competing effects due to matrix viscoelasticity on drop migration are identified. The first stems from the reduced inclination angle of the drop with increasing viscoelasticity that tries to enhance migration velocity. However, it is overcome by the second effect inhibiting migration that results from the normal stress differences from the curved streamlines around the drop; they are more curved on the side away from the wall compared with those in the gap between the wall and the drop, an effect that is also present for a rigid particle. A perturbative theory of migration is developed for small ratio of the drop size to its separation from the wall that clearly shows the migration to be caused by the image stresslet field due to the drop in presence of the wall. The theory delineates the two competing viscoelastic effects, their relative magnitudes, and predicts migration that matches well with the simulation. Using the simulation results and the stresslet theory, we develop an algebraic expression for the quasi-steady migration velocity as a function of *Ca*, *De* and β. The transient dynamics of the migrating drop is seen to be governed by the finite time needed for development of the viscoelastic stresses. For larger capillary numbers, in both Newtonian and viscoelastic matrices, a viscous drop fails to reach a quasi-steady state independent of initial drop–wall separation. Matrix viscoelasticity tends to prevent drop breakup. Drops that

† Email address for correspondence: sarkar@gwu.edu

break up in a Newtonian matrix are stabilized in a viscoelastic matrix if it is initially far away from the wall. Initial proximity to the wall enhances deformation and aids in drop breakup.

Key words: complex fluids, drops, viscoelasticity

---

1. Introduction

In a wall-bounded shear flow, a spherical particle does not experience any lateral motion across streamlines in the absence of inertia due to the reversibility of Stokes flow (Saffman 1956; Bretherton 1962; Leal 2007). However, in the case of a viscous drop, deformation destroys the fore–aft symmetry and thereby the reversibility. The deformed particle experiences a lift and migrates away from the wall. Migration can also be induced by effects other than deformation (i.e. inertia and viscoelasticity) that also break the symmetry. Here, we numerically investigate the migration of a sheared viscous drop near a wall in a viscoelastic liquid.

Migration of particles plays a critical role in many situations. In polymer processing, it can generate a non-uniform filler distribution (Hegler & Mennig 1985). In blood flow, it is responsible for the reduction of hematocrit (Fahraeus effect) and apparent viscosity (Fahraeus–Lindqvist effect) in smaller capillaries and margination of white blood cells, a crucial step in leukocyte cascade and thereby the immune response (Tangelder *et al.* 1985). For purely viscous systems, lateral migration of wall-bounded particles and drops has been investigated in many experiments and theoretical studies considering a number of different effects: single versus two walls, effects of inertia and gradient of shear rate (e.g. in Poiseuille flow); see the review by Leal (1980) for research prior to 1980. For a wall-bounded simple shear, migration of a viscous drop away from the wall was seen by Goldsmith & Mason (1962) and was theoretically predicted by Chaffey, Brenner & Mason (1965) using a first-order perturbative theory, which was subsequently experimentally validated by Karnis & Mason (1967). The perturbative analysis was extended by Chan & Leal (1979) to cases involving two walls, the presence of shear rate gradient and a viscoelastic second-order suspending fluid. More recently, Smart & Leighton (1991) developed an elegant theoretical result relating drift of a drop away from a wall to the stresslet field due to the drop and the resulting normal stresses in a dilute emulsion. They successfully compared it with the drift measured in a Couette device. Migration was numerically simulated using boundary element method (BEM) and compared with analytical results (Uijttewaal, Nijhof & Heethar 1993; Kennedy, Pozrikidis & Skalak 1994) to show that the latter lose accuracy for small wall distance and large deformation, as well as when the transient time scale of deformation is much larger than that of migration.

Non-Newtonian effects can profoundly change particle motion. Saffman (1956) first suggested that the indeterminacy in the Stokes flow – spheroidal particles are predicted to move in Jeffrey's orbits (Jeffery 1922) decided by their orientation at the initial instant, while experimentally they were observed to take up preferred orientation – can be resolved in presence of non-Newtonian effects of the surrounding medium. Karnis & Mason (1966) experimentally observed that solid spheres migrate towards the outer wall in a Couette flow of viscoelastic fluids. Mason's group performed a number of detailed investigations of particle and drop motion in viscoelastic Couette and

Poiseuille flows (Gauthier, Goldsmith & Mason 1971*a*,*b*; Bartram, Goldsmith & Mason 1975). In a Poiseuille flow, rigid particles move towards the centre line in a viscoelastic liquid, but towards the wall in a viscous shear-thinning liquid; drops also move towards the centre line in a viscoelastic liquid but to an intermediate position between wall and the centre line in a viscous shear thinning liquid. Migration of a rigid sphere in a second-order fluid was analysed using a perturbation method by Leal and coworkers (Ho & Leal 1976; Chan & Leal 1977) to obtain qualitative agreement with the experimental observation that a sphere moves towards minimum shear rate, and therefore no migration in a pure shear due to absence of shear rate gradient. The authors later analysed the case of a slightly deformed drop (Chan & Leal 1979). Here, the perturbation was extended to a higher order (in the ratio of drop radius to the gap width) that predicted a migration of rigid sphere away from the wall even in a constant shear flow. The authors also concluded that the disagreement between the prediction from the perturbation study and the experiments indicated inadequacy of the second-order fluid model to account for strong viscoelastic effects in presence of walls (see the excellent review of particle motions in non-Newtonian fluids by Leal (1979)). In the 1990s, Feng and Joseph performed detailed experimental and numerical investigation of particle motion in viscoelastic fluids studying different shapes of particles, effects of confinement as well as inertia. Feng & Joseph (1996) found that spheres migrate outward in a torsional flow between two discs under the action of normal stresses, whereas rods migrate inward or outward depending on their motion along Jeffrey's orbits or aligned with streamlines. They analysed the forces in a second-order fluid to show that a particle experiences compressive forces due to normal stresses that tend to align long bodies with the flow direction, move cylinders towards wall and aggregate them (Joseph & Feng 1996). Huang *et al.* (1997) simulated two-dimensional motion of rigid cylinders in an Oldroyd-B fluid (along with Carreau–Bird shear thinning) to find that the migration and the eventual equilibrium position depend on inertia, viscoelasticity, shear thinning and the blockage ratio (effects of both bounding walls). At low Reynolds numbers, viscoelastic normal stresses drive particles towards one of the walls. Shear thinning increases the shear rate in regions of constant shear stress, and therefore normal stresses increase enhancing the effects. More recently, finite-element simulation showed that rigid spheres in a shear flow of Giesekus liquid migrate to the closest wall in both two and three dimensions (D'Avino *et al.* 2010*a*,*b*). Such wall-ward migration was also experimentally observed in oscillatory Couette flows (Lormand & Phillips 2004) at low frequencies. Increasing frequency of oscillation however introduces more complex behaviour.

In contrast to rigid particles, there has been no numerical simulation of viscoelastic effects on drop migration. The only analysis of this phenomenon is the small deformation perturbative study using a second-order fluid by Chan & Leal (1979), where, as we mentioned above, the authors noted the inadequacy of the model. It predicted that both drop and matrix viscoelasticity promotes migration away from walls in contrast to other studies as well as the numerical results to be presented below. They also did not see much difference in response between the two cases (viscoelastic drop or matrix phase). This also contrasts with recent experimental and numerical findings about drop response in unbounded shear (Aggarwal & Sarkar 2007, 2008*b*). Drop deformation itself induces migration away from the wall in a Newtonian medium. From the experimental and numerical literature for rigid particles, one would expect viscoelastic effects to compete against it. However, viscoelastic effects are subtle, and

the intuition about them is severely limited. For instance, there has been disagreement in the literature even for simple questions such as whether viscoelasticity increases or decreases drop deformation in shear (Tavgac 1972; Flumerfelt 1972; Elmendorp & Maalcke 1985). Numerical simulation (Yue *et al.* 2005; Aggarwal & Sarkar 2008*a*) recently resolved this issue by demonstrating that the response of a sheared viscous drop in a viscoelastic matrix is non-monotonic. The detailed simulation could explain the reason behind the non-monotonicity (Aggarwal & Sarkar 2008*a*): increasing viscoelasticity decreases drop inclination leading it away from the extensional axis at 45° causing decreased deformation, but further increase of viscoelasticity gives rise to a strong extensional flow at drop tips that eventually increases deformation. Note that the perturbative study mentioned above (Chan & Leal 1979) assumed that the drop remains aligned with the extensional axis of the shear flow at 45°. We will see below that the deviation of the inclination from this angle due to viscoelasticity plays an interesting role in the migration. We would also see here that the effect of matrix viscoelasticity on drop migration is a result of subtle competition between two effects which *a posteriori* justifies an attempt at a careful numerical and theoretical analysis presented here.

In order to understand the complex phenomenon of viscoelastic effects on migration, here we choose the simplest realizable problem that involves migration of a deforming drop in presence of viscoelasticity: a three-dimensional simulation of a viscous drop in a shear flow near a wall in a viscoelastic medium. We use a front-tracking finite difference method (Tryggvason *et al.* 2001) that has been used in our lab for a number of viscous (Sarkar & Schowalter 2001; Li & Sarkar 2005*a*,*b*,*c*, 2006; Olapade, Singh & Sarkar 2009; Singh & Sarkar 2011) and viscoelastic (Sarkar & Schowalter 2000; Aggarwal & Sarkar 2007, 2008*a*,*b*; Mukherjee & Sarkar 2009, 2010, 2011) drop problems. Our previous studies used Oldroyd-B model for viscoelasticity. Here we choose a modified version of the Chilcott–Rallison (CR)-type finitely extensible nonlinear elastic (FENE) model (Chilcott & Rallison 1988). Unlike the Oldroyd-B model, this model has a finite extensional viscosity and a constant shear viscosity. It models Boger fluids and has been used in many viscoelastic studies (Szabo, Rallison & Hinch 1997; Ramaswamy & Leal 1999; Dou & Phan-Thien 2003; Kim *et al.* 2005). The modified FENE-CR, also known as FENE-MCR, gives identical responses in simple steady shear as FENE-CR, the only difference between the two models arising in very strong convective flows (Matos, Alves & Oliveira 2009). FENE-MCR has also been widely used in the literature, e.g. for viscoelastic flows through axisymmetric contractions (Coates, Armstrong & Brown 1992), viscoelastic flows at a T-junction (Matos *et al.* 2009), bifurcation phenomena in viscoelastic flows (Rocha, Poole & Oliveira 2007), viscoelastic flows past cylinders (Oliveira & Miranda 2005), two-dimensional vortex dynamics in a cylinder wake (Sahin & Owens 2004; Moyers-Gonzalez & Frigaard 2010) and studies of the plane Couette–Poiseuille flow (Moyers-Gonzalez & Frigaard 2010). In the following, mathematical formulation and numerical implementation are described in § 2. In § 3 we describe the problem set-up and method convergence. In § 4 we discuss numerical results. We also develop a theory for drop migration, and compare it with numerical results and provide an algebraic expression of migration. Section 5 concludes the work.

2. Mathematical formulation and numerical implementation

We have previously described the mathematical formulation underlying our computational tool for simulating drops with viscoelastic constitutive equations

(Aggarwal & Sarkar 2007, 2008a; Mukherjee & Sarkar 2009, 2010, 2011). The (droplet-matrix) system is governed by the incompressible momentum conservation equations:

$$\frac{\partial(\rho\boldsymbol{u})}{\partial t} + \nabla \cdot (\rho\boldsymbol{uu}) = \nabla \cdot \boldsymbol{\tau} - \int_{\partial B} \mathrm{d}\boldsymbol{x}_B \kappa \boldsymbol{n} \Gamma \delta(\boldsymbol{x} - \boldsymbol{x}_B), \tag{2.1}$$

$$\nabla \cdot \boldsymbol{u} = \boldsymbol{0} \tag{2.2}$$

in the entire domain Ω. The total stress $\boldsymbol{\tau}$ is decomposed into pressure, polymeric and viscous parts:

$$\boldsymbol{\tau} = -p\boldsymbol{I} + \boldsymbol{T}^p + \boldsymbol{T}^v, \quad \boldsymbol{T}^v = \mu_s \boldsymbol{D}, \tag{2.3}$$

where p is the pressure, μ_s is the solvent viscosity and $\boldsymbol{D} = (\nabla\boldsymbol{u}) + (\nabla\boldsymbol{u})^{\mathrm{T}}$ is the deformation rate tensor. The superscript 'T' represents the transpose. Here $\boldsymbol{T}^p$ is the extra stress (or viscoelastic stress) due to the presence of polymer. In (2.1) Γ is the interfacial tension (constant), ∂B represents the surface of the drop consisting of points $\boldsymbol{x}_B$, κ the local curvature, $\boldsymbol{n}$ the outward normal and $\delta(\boldsymbol{x} - \boldsymbol{x}_B)$ is the three-dimensional Dirac delta function. The FENE-CR constitutive equation in terms of the conformation tensor $\boldsymbol{A}$ is given by

$$\frac{\partial\boldsymbol{A}}{\partial t} + \boldsymbol{u} \cdot \nabla\boldsymbol{A} = \nabla\boldsymbol{u} \cdot \boldsymbol{A} + \boldsymbol{A} \cdot (\nabla\boldsymbol{u})^{\mathrm{T}} - \frac{f}{\lambda}(\boldsymbol{A} - \boldsymbol{I}) \quad \text{where } f = \frac{L^2}{L^2 - \mathrm{tr}(\boldsymbol{A})}. \tag{2.4}$$

The relation between the stress $\boldsymbol{T}^p$ and conformation tensor $\boldsymbol{A}$ is

$$\boldsymbol{A} = \left(\frac{\lambda}{\mu_p f}\right)\boldsymbol{T}^p + \boldsymbol{I}. \tag{2.5}$$

One can obtain an equation for the extra stress $\boldsymbol{T}^p$:

$$\frac{\partial\boldsymbol{T}^p}{\partial t} + \left\{\boldsymbol{u} \cdot \nabla\boldsymbol{T}^p - \nabla\boldsymbol{u} \cdot \boldsymbol{T}^p - \boldsymbol{T}^p \cdot \nabla\boldsymbol{u}^{\mathrm{T}}\right\} + f\boldsymbol{T}^p\left[\frac{\partial}{\partial t}\left(\frac{1}{f}\right) + \boldsymbol{u} \cdot \nabla\left(\frac{1}{f}\right)\right] + \frac{f}{\lambda}\boldsymbol{T}^p$$

$$= \frac{f}{\lambda}\mu_p\boldsymbol{D},$$

$$f = \frac{L^2 + \dfrac{\lambda}{\mu_p}\left(\sum T_{ii}^p\right)}{L^2 - 3}. \tag{2.6}$$

Here μ_p is the polymeric viscosity, λ is the relaxation time and L is the finite extensibility. The FENE-CR model introduces finite extensibility L which limits the maximum length of the end-to-end vector for the polymer molecule. In the limit of $L \to \infty$ we obtain the Oldroyd-B equation. To obtain an explicit elastic viscous splitting, we follow the finite analytic integration technique developed in our previous work (Sarkar & Schowalter 2000); equation (2.6) can be expressed as

$$\frac{\partial\boldsymbol{T}^p}{\partial t} + \frac{f}{\lambda}\boldsymbol{T}^p = \boldsymbol{K}(t), \tag{2.7}$$

where

$$\boldsymbol{K}(t) = \frac{f}{\lambda}\mu_p\boldsymbol{D} - \left\{\boldsymbol{u} \cdot \nabla\boldsymbol{T}^p - \nabla\boldsymbol{u} \cdot \boldsymbol{T}^p - \boldsymbol{T}^p \cdot \nabla\boldsymbol{u}^{\mathrm{T}}\right\} - f\boldsymbol{T}^p\left[\frac{\partial}{\partial t}\left(\frac{1}{f}\right) + \boldsymbol{u} \cdot \nabla\left(\frac{1}{f}\right)\right]. \tag{2.8}$$

It is integrated over a time step t^n to t^{n+1} to result in the following expressions

$$
(\boldsymbol{T}^p)^{n+1} - (\boldsymbol{T}^p)^n \mathrm{e}^{-(f/\lambda)\Delta t} = \mathrm{e}^{-(f/\lambda)t^{n+1}} \int_{t^n}^{t^{n+1}} [\boldsymbol{K}(t)] \mathrm{e}^{(f/\lambda)t} \, \mathrm{d}t
$$

$$
= \mathrm{e}^{-(f/\lambda)t^{n+1}} \left[\frac{\lambda}{f} \mathrm{e}^{-(f/\lambda)t} \boldsymbol{K}(t) \right]_{t^n}^{t^{n+1}}
$$

$$
- \mathrm{e}^{-(f/\lambda)t^{n+1}} \frac{\lambda}{f} \int_{t^n}^{t^{n+1}} \left[\frac{\partial \boldsymbol{K}(t)}{\partial t} \mathrm{e}^{-(f/\lambda)t} \right] \mathrm{d}t
$$

$$
\approx \frac{\lambda}{f} [1 - \mathrm{e}^{-(f/\lambda)\Delta t}] \boldsymbol{K}^n, \tag{2.9}
$$

where we have assumed $K^n \approx K^{n+1}$. Note that it offers an automatic elastic viscous stress splitting

$$
(\boldsymbol{T}^p)^{n+1} = \mu_p \boldsymbol{D}^n + \left[(\boldsymbol{T}^p)^n - (\mu_p \boldsymbol{D})^n \right] \mathrm{e}^{-(f/\lambda)\Delta t} + \frac{\lambda}{f} \left[1 - \mathrm{e}^{-(f/\lambda)\Delta t} \right] (\boldsymbol{K}^n - \mu_p \boldsymbol{D}^n). \tag{2.10}
$$

The effects of the terms $\partial(1/f)/\partial t$ and $\boldsymbol{u} \cdot \nabla(1/f)$ are neglected resulting in the FENE-MCR equation:

$$
(\boldsymbol{T}^p)^{n+1} = \mu_p \boldsymbol{D}^n + \left[(\boldsymbol{T}^p)^n - \mu_p \boldsymbol{D}^n \right] \mathrm{e}^{-(f/\lambda)\Delta t} - \frac{\lambda}{f} [\boldsymbol{u} \cdot \nabla \boldsymbol{T}^p - \nabla \boldsymbol{u} \cdot \boldsymbol{T}^p - \boldsymbol{T}^p \cdot \nabla \boldsymbol{u}^{\mathrm{T}}]^n
$$

$$
+ \mu_p \boldsymbol{D}^n \left[1 - \mathrm{e}^{-(f/\lambda)\Delta t} \right]. \tag{2.11}
$$

Keeping those terms resulted in little difference. The drop is described by a triangulated front distinct from the regular Cartesian grid used to solve the flow field; the front is adaptively regridded to prevent excessive distortion of the front elements. A multigrid method is used for the pressure Poisson equation, and an alternating direction implicit (ADI) method is used for the viscous terms $(\mu_p + \mu_s)\boldsymbol{D}$ to alleviate the diffusion restriction on the time step. The above algorithm therefore was used to compute the non-Newtonian part of the stress $\boldsymbol{T}^{NN} = \boldsymbol{T}^p - \mu_p \boldsymbol{D}$. Other details can be found in the previous papers (Sarkar & Schowalter 2000, 2001; Li & Sarkar 2006; Aggarwal & Sarkar 2007).

3. Problem set-up and convergence

At $t = 0$, a spherical drop of radius a is placed in a computational domain. The size of the domain is $L_x = 10a$, $L_y = 10a$ and $L_z = 5a$. The upper plate (y direction domain boundary) is impulsively started (in the x direction) with a velocity $2U$, and the lower plate is kept stationary creating a shear rate of $\dot{\gamma} = 2U/L_y$. The drop is positioned in close proximity to the lower stationary wall and the initial distance (h_i) is varied. We use a and $\dot{\gamma}^{-1}$ as the non-dimensionalizing length and time scales, respectively. The dimensionless parameters are Reynolds number $Re = \rho_m a^2 \dot{\gamma}/\mu_m$ capillary number $Ca = \mu_m a \dot{\gamma}/\Gamma$, Deborah number (or Wissenberg number) $De = \lambda \dot{\gamma}$, viscosity ratio $\lambda_\mu = \mu_d/\mu_m$, density ratio and $\beta = \mu_{pm}/\mu_m$ is the ratio of the polymeric to the total matrix viscosity. The subscript d and m refer to the drop and the matrix phases. The total viscosity of the matrix is given as $\mu_m = \mu_{sm} + \mu_{pm}$, sum of the solvent and polymeric viscosities. In all our simulations, viscosity and density ratios are kept fixed at unity. We have chosen $\beta = 0.5$ and FENE-MCR limiting length $L = 20$ for all computations, unless otherwise mentioned, e.g. where we study the effects
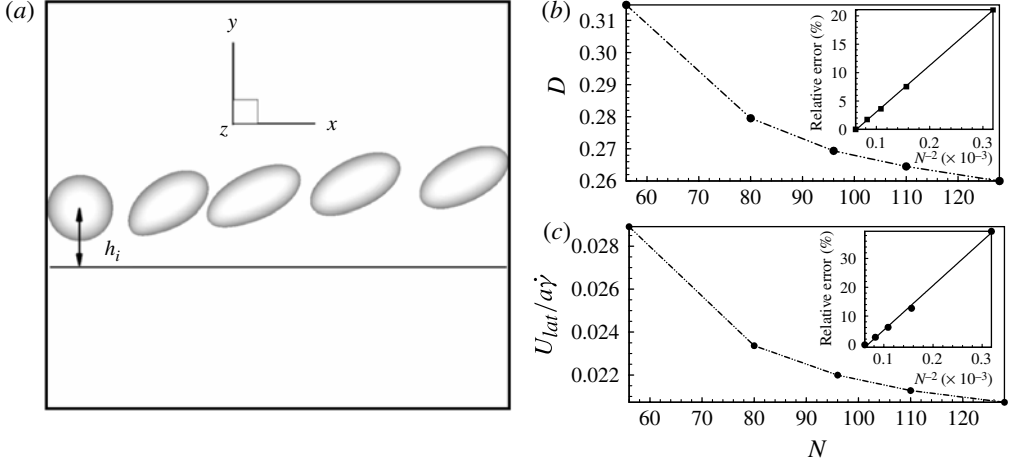
FIGURE 1. (*a*) Qualitative representation of a migrating drop (h_i is the initial drop-to-wall distance). Grid convergence study of the drop deformation (*b*) and lateral migration velocity (*c*) for $Ca = 0.2$, $De = 0.75$ and $h_i/a = 1.35$. Here N is the number of grid points in the x direction. Relative errors compared with the highest grid density are shown in the insets.

of these parameters. The explicit nature of the code restricts us (despite the ADI implementation of the viscous terms) to a small non-zero Reynolds number of 0.03, where inertial effects are negligible. Figure 1(*a*) shows a schematic of a drop migrating in a shear flow away from a wall (drawn from actual simulation but the horizontal distance is shortened to exaggerate the motion).

Convergence of the algorithm using the Oldroyd-B constitutive relation has been established in our previous publications (Aggarwal & Sarkar 2007, 2008*a*; Mukherjee & Sarkar 2009, 2010, 2011) on drop deformation. Here we investigate the grid independence for the migration problem. Figure 1(*b,c*) plot the deformation and lateral migration velocities of a Newtonian drop migrating in a viscoelastic media for increasing discretization levels for $Ca = 0.2$, $De = 0.75$, $L = 20$. The grid resolution ($\Delta x = \Delta y = \Delta z$) is varied from $a/5.6$ ($N = 56$) to $a/12.8$ ($N = 128$) where a is the drop radius. We note that the deformation and velocity do not vary much beyond the discretization level of $a/9.6$. In the inset, the relative changes with respect to the highest grid resolution at a particular time instant are plotted. At $\Delta x = a/9.6$, error in the velocity is around 4.5 %, and in the interest of achieving a reasonable computational time, we choose ($96 \times 96 \times 48$) as our grid resolution for all further simulations.

4. Results

4.1. *Newtonian lateral migration and comparison*

As mentioned before, a viscous drop suspended in a viscous shear flow deforms, changes its orientation angle and moves laterally away from a nearby wall. An initially spherical drop becomes ellipsoidal thereby breaking the symmetry in its shape in the presence of the wall. It experiences an extra drag and lift of purely viscous origin, and starts migrating laterally away from the wall. The drop quickly reaches a steady state where its motion does not depend on the initial position. For a Newtonian case, we compare quasi-steady migration velocities from our simulations with those obtained
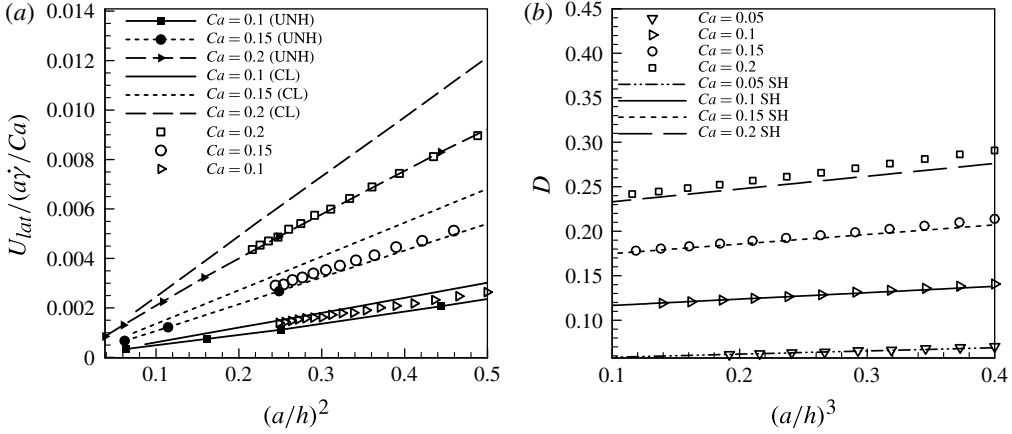
FIGURE 2. (*a*) Comparison of simulated lateral migration velocity with Chan and Leal (CL) and Uijttewaaal et al. (UNH). (*b*) Comparison of the deformation parameter with Shapira and Haber (SH). In the formula of Shapira and Haber, D_{Taylor} has been replaced by the deformation parameter of unbounded cases from our simulations.

from a perturbative theory (Chan & Leal 1979) and a BEM simulation (Uijttewaal *et al.* 1993) in figure 2(*a*). The perturbation expression for lateral migration is

$$\frac{U_{lat}}{a\dot{\gamma}} = D_{Taylor} \left(\frac{3(54\lambda^2 + 97\lambda + 54)}{280(1 + \lambda)^2} \right) \left(\frac{a}{h} \right)^2. \tag{4.1}$$

We note that the simulated migration velocity is in good agreement with the theory for low values of capillary numbers, where the perturbation analysis is valid. As *Ca* is increased (*Ca* = 0.2), our simulation matches with BEM simulation (Uijttewaal *et al.* 1993) better. In conformity with the analytical result (4.1), our simulation shows a linear variation of migration velocity with the inverse of square of the distance from the wall. In figure 2(*b*) we compare deformation in presence of a nearby wall with the theoretical expression of Shapira & Haber (1990):

$$D_{SH} = D_{Taylor} \left(1 + \frac{3}{8} \left(\frac{a}{h} \right)^3 \left[\frac{1 + 2.5\lambda_\mu}{1 + \lambda_\mu} \right] \right). \tag{4.2}$$

We replaced the Taylor deformation in (4.2) by the deformation simulated here to achieve a slightly better match. After thus validating our simulation tool against previous results, we introduce viscoelasticity in the matrix and investigate its effects in detail.

4.2. *Effects of Deborah number, polymeric viscosity and extensibility*

A viscoelastic matrix slows down the migration process. In this section, we choose a moderate capillary number of *Ca* = 0.2. Figure 3(*a*) plots lateral migration velocity for four initial drop positions for a Newtonian and a non-Newtonian case. We note that the viscoelasticity in the matrix reduces the migration velocity considerably, even for a small *De* number of 0.5. Note that after the initial transients the reduced quasi-steady drop velocity in a viscoelastic matrix depends only on its current distance from the wall and all of them collapse on a single curve irrespective of the initial starting position, just like in a Newtonian case. In the inset we show that the quasi-steady
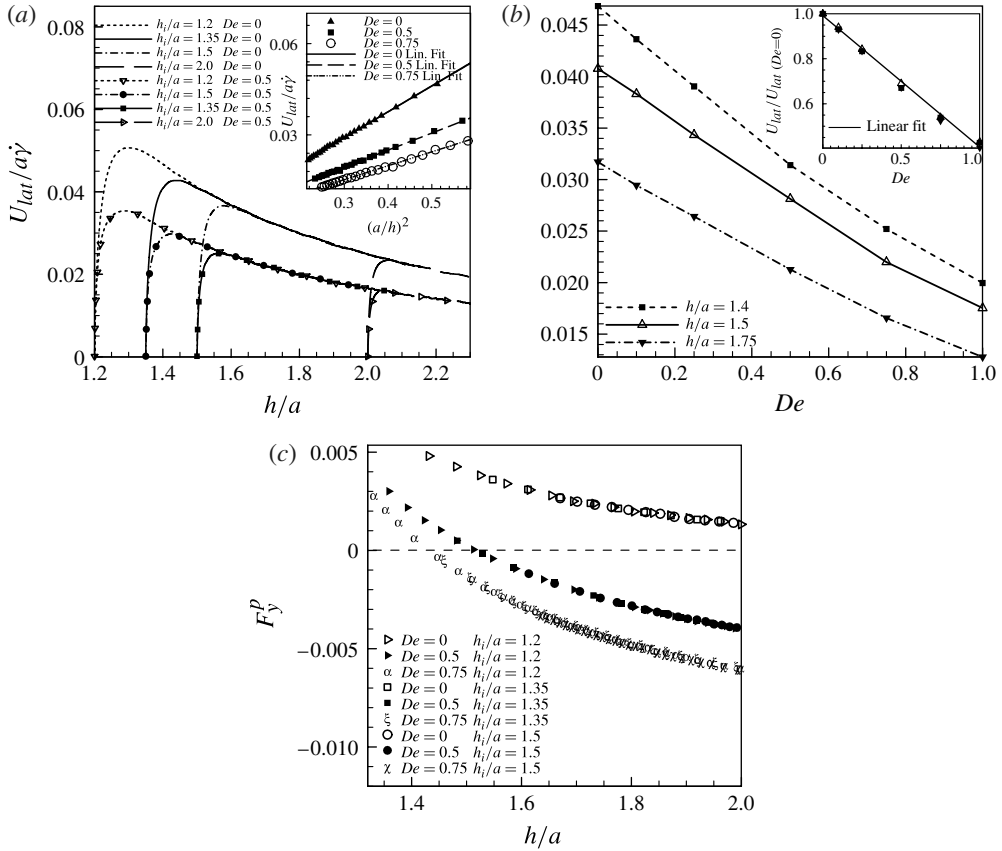
FIGURE 3. (*a*) Evolution of lateral migration velocity versus the distance of the drop from the wall for varying *De* and initial drop height (h_i/a) for $Ca = 0.2$. The inset shows quasi-steady velocities varying linearly with the inverse of the square of the instantaneous wall distance for different *De* values. (*b*) Quasi-steady lateral migration velocities versus *De* for varying drop distances from the wall and $Ca = 0.2$. The inset shows the same migration velocity normalized by their corresponding Newtonian values all collapsing on a single curve. (*c*) Quasi-steady viscoelastic net force on the drop versus the distance of the drop from the wall for varying *De*, $Ca = 0.2$ and three different initial drop heights.

velocity scales with the inverse of the square of the distance of the drop centre from the wall for different *De*. A linear fit for each *De* is also shown. Note that the independence of the migration velocity on the initial position is in conformity with the Stokes flow results (Leal 1979). Recent finite-element simulation also showed that the migration of a rigid sphere in a viscoelastic matrix and the long-time dynamics are independent of the initial position (D'Avino *et al.* 2010*a*). In the following, we will concentrate on the quasi-steady dynamics and investigate transient effects and breakup in §§ 4.6 and 4.7, respectively.

In figure 3(*b*), we plot the quasi-steady lateral migration velocity as a function of *De* for several instantaneous wall to drop distances for $Ca = 0.2$. For larger wall distances, the curves are approximately linear with slight deviation only when the drop is close to the wall or for larger *De* values ($De \geqslant 0.75$). This variation is due to the formation of stretched drop tip close to the wall. It happens only at a very small

drop-to-wall distance due to the high viscoelastic stresses in the locally extensional flow. We discuss this phenomenon below. The inset of figure 3(*b*) shows that when the velocity is normalized by its Newtonian value, all of them collapse on a single linear curve. The effect of viscoelasticity on the slip velocity is extremely small at $Ca = 0.2$, and therefore, will be investigated at other capillary numbers in the next subsection.

In figure 3(*c*), we plot the vertical component of the viscoelastic force ($\int_{\partial B} (\boldsymbol{n} \cdot \boldsymbol{T}^p)\, \mathrm{d}a$, where $\boldsymbol{n}$ is the normal to the drop surface ∂B) on the drop versus the instantaneous distance from the wall, after the quasi-steady state has been reached for three different initial heights and Deborah numbers. Again we note that the force curve for a particular Deborah number becomes independent of the initial drop height and depends only on the instantaneous position. We also note that the nominally viscoelastic force is positive for a Newtonian case ($e \rightarrow 0$) where the viscoelastic stress is $\mu_p \boldsymbol{D}$. With a finite non-zero Deborah number, it becomes eventually negative as the part $\lambda \left\{ \boldsymbol{u} \cdot \nabla \boldsymbol{T}^p - \nabla \boldsymbol{u} \cdot \boldsymbol{T}^p - \boldsymbol{T}^p \cdot \nabla \boldsymbol{u}^{\mathrm{T}} \right\}$ in (2.6) dominates $\mu_p \boldsymbol{D}$ indicating a retarding effect of viscoelasticity on the migration. As noted before, the shape asymmetry of the deformed drop relative to the wall gives rise to the migration away from the wall.

In figure 4(*a*), we plot deformation for varying De at $Ca = 0.2$ for two different initial drop heights ($h_i/a = 1.2$ and $h_i/a = 1.5$). Similar to the migration velocity, in the quasi-steady state, deformation also becomes independent of the initial drop position. With increasing De, the drop deformation first decreases for $De = 0.1$ and 0.5 and then increases beyond that. This can be seen clearly in figure 4(*b*) where quasi-steady deformations normalized by the respective Newtonian values, are plotted as a function of De, at several drop heights for three different initial drop heights ($h_i/a = 1.2, 1.35, 1.5$). We notice that the deformation parameters are increasing beyond $De = 0.5$. This non-monotonicity is due to the presence of two competing effects, the decreasing orientation angle and increasing viscoelastic stresses at the tip, as was shown previously by our group (Aggarwal & Sarkar 2008*a*). As De is increased, initially the deformation decreases due to decreasing inclination angle, resulting in the drop moving away from the extensional axis, but with further increase in De the deformation increases because of the increasing extensional viscoelastic stresses at the tips which become dominant for higher De values. The curves also collapse on each other up to the Deborah number where non-monotonicity appears. In figure 4(*c*), we plot inclination angle versus $(a/h)^2$ for two initial drop heights and four Deborah numbers. Note that Uijttewaal *et al.* (1993) provided such a plot for the viscous system; perturbative theories indicate an $(a/h)^2$ dependence for deformation and migration velocities, but not for the inclination angle. Here, we see a slight decrease with $(a/h)^2$; interaction with the wall tend to align the drop in the flow direction. The inclination angle in the quasi-steady state, like velocity and deformation, does not depend on the initial drop height, and curves for a particular De are on top of each other. As we saw for the unbounded drop case, the drop inclination angle decreases linearly with De (Aggarwal & Sarkar 2008*a*). Upon normalizing the angle with values at $De = 0$, we note that the normalized angles all collapse on one straight line with De for three different instantaneous drop heights (inset of figure 4*c*). In figure 4(*d*), we show the drop shape and the streamlines around it. Note that the streamlines above the drop are more curved and therefore viscoelastic tensile stresses are larger compared with those below the drop resulting in a net downward force on the drop that retards migration. The viscoelastic normal stress due to curvature of the surrounding streamlines is the primary reason of hindered migration. The same effect was also noted by Joseph and coworkers (Huang *et al.* 1997) for a rigid sphere in shear flow migrating towards a wall. There is a second effect which stems from drop
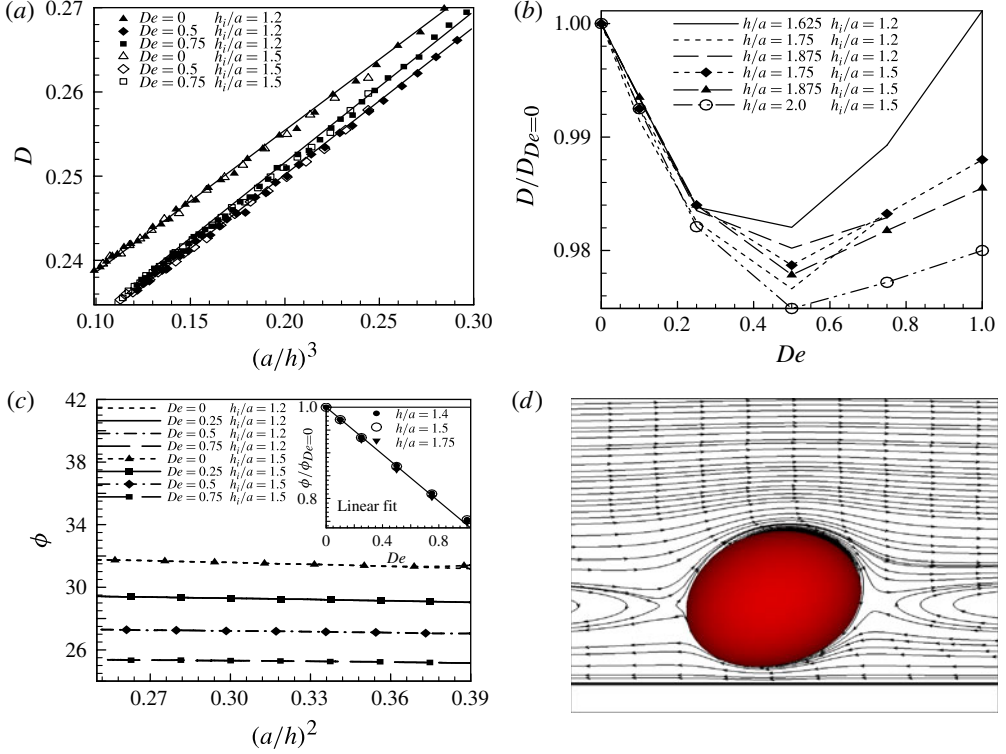
FIGURE 4. (Colour online) (*a*) Quasi-steady deformation versus the inverse of the cube of the drop-to-wall distance for varying *De* for $Ca = 0.2$ and two different initial heights. (*b*) Deformation normalized by their corresponding Newtonian values versus *De* for $h_i/a = 1.2$, 1.35 and 1.5 at three different instantaneous heights for the same capillary number. (*c*) Inclination angle versus the inverse of the square of the drop-to-wall distance for various *De*, $Ca = 0.2$, $h_i/a = 1.2$ and 1.5. The inset shows the normalized angle with varying Deborah number at three different instantaneous heights. (*d*) Streamlines around a drop for $h/a = 1.2$ for $De = 0.75$ and $Ca = 0.05$. The coordinate system is translating with the drop with its velocity in the *x* direction.

deformation absent in rigid sphere case: more specifically related to the decreasing angle of inclination (increasing drop alignment with the flow) of the deformed drop that tends to increase migration. We investigate this phenomenon in detail in § 4.4 below.

In figure 5, we investigate viscous and viscoelastic forces per unit volume in the vertical direction along the surface in the normal direction for varying *De* and $Ca = 0.2$ as a function of angular position in the midplane $z = L_z/2$ at a non-dimensional height of 1.5. Here $\phi_1 = 0$ corresponds to the *x*-axis; drop tips are shown in each figure. These quantities are interpolated from the three-dimensional grid to the front grid using the same interpolating function used in the front tracking implementation. Note that these are the forces per unit volume $\nabla \cdot \boldsymbol{\tau}$ due to viscous and polymeric contribution that directly appear in the momentum equation (2.1). In the limit of $De \to 0$ the viscoelastic stress is $\mu_p \boldsymbol{D}$. In figure 5(*a*), viscous vertical forces ($F_y^{vis} = \hat{\boldsymbol{y}} \cdot (\nabla \cdot \mu_s \boldsymbol{D})$) are plotted. We note that as viscoelasticity is increased, the viscous forces around the drop increase except in a very small region around $\phi_1 \approx -0.6\pi$
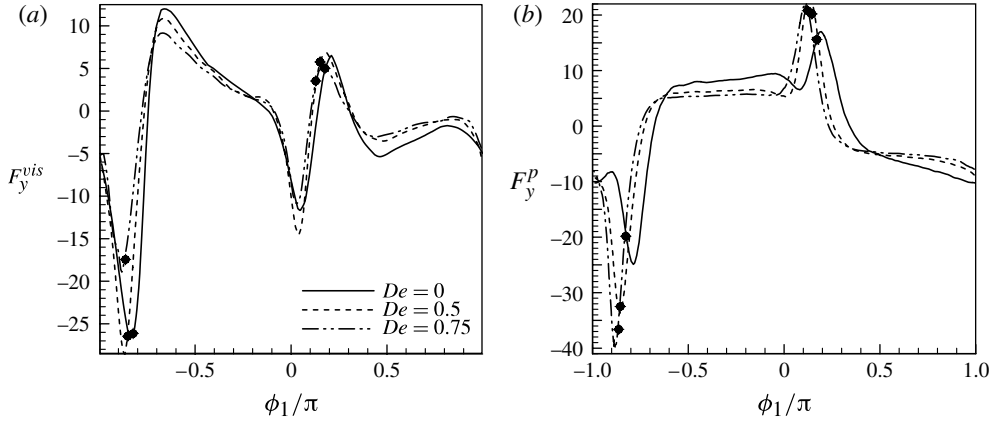
FIGURE 5. Viscous forces $F_y^{vis} = \hat{\boldsymbol{y}} \cdot (\boldsymbol{\nabla} \cdot \mu_s \boldsymbol{D})$ (*a*) and viscoelastic forces $F_y^p = \hat{\boldsymbol{y}} \cdot (\boldsymbol{\nabla} \cdot \boldsymbol{T}^P)$ (*b*) in the vertical direction along the circumference of the drop in the central $z = L_z/2$ plane plotted as a function of the angular position ($\phi_1 = 0$ coincides with *x*-axis) for different *De* at $Ca = 0.2$ and $h/a = 1.5$.

(peak region of the curves). This indicates that the change due to viscoelasticity in viscous stress promotes lateral migration of the drop away from the wall; in § 4.4, this observation will be substantiated by a semi-analytical theory. In figure 5(*b*) we plot viscoelastic vertical forces F_y^p along the circumference of the drop. We note that in the region approximately between -0.7π and 0.3π the vertical force is positive, indicating force pushing away from the wall ($\phi_1 \approx -0.7\pi$ refers to the location where the drop surface is closest to the wall). However, outside this region F_y^p is negative and pulls the drop towards the wall. We note that as *De* is increased, F_y^p sharply becomes more negative in the region where the matrix fluid is squeezed between the drop and the wall, hindering migration away from the wall. Although the tip away from the wall experiences larger push as *De* is increased, that closer to the wall has much stronger pull towards it. Cantat & Misbah (1999) plotted the total vertical hydrodynamics force distribution under a vesicle migrating in a shear flow of viscous liquid. Although the situation with the vesicle there differs from the drop here, in having extra bending and adhesion forces resulting in a very different shape, and consequently the maximum values at locations different from the drop, a qualitative similarity in the nature of the forces can be noted. These vertical forces are directly responsible for the decreased lateral migration of a drop in a viscoelastic matrix. Viscoelastic normal traction force along the circumference (not shown here for brevity) is extensional at the tip and compressive at the equator; both are responsible for the deformation of the drop, although forces at the tip are much more dominant. Also the force has higher values at the tip closer to the wall leading to excess deformation. It increases dramatically, particularly at the lower tip, as *De* is increased.

Next we study the effects of variation of the amount of polymeric viscosity by varying the parameter β. In figure 6(*a*), we plot the migration velocity for varying *De* for several β values, respectively. When it is plotted against βDe (in the inset), we find a linear scaling. We briefly study the effects of varying the maximum polymer length (*L*, also known as the maximum extensibility) by plotting deformation, inclination and the lateral migration velocity normalized by the respective Newtonian values in figure 6(*b*) for $Ca = 0.2$, $De = 0.75$, $h/a = 1.5$. We note that as it increased, velocity
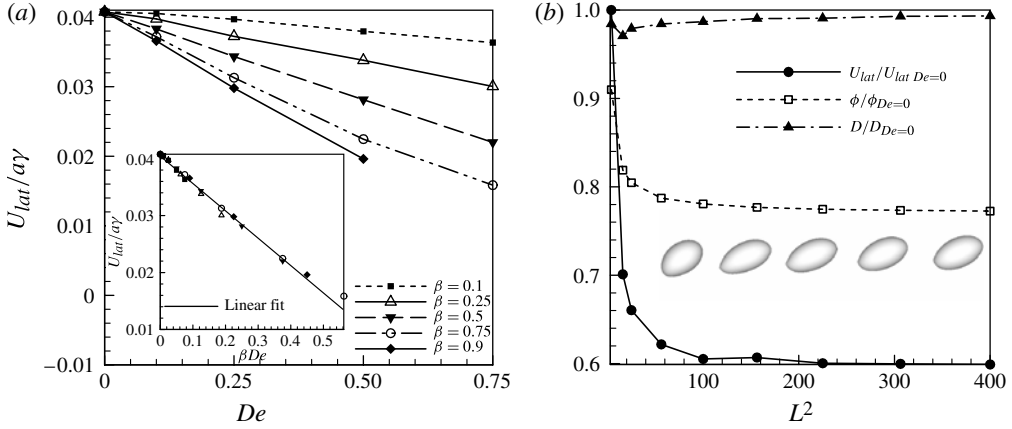
FIGURE 6. (*a*) Migration velocity plotted for varying *De* for different *β* values at *Ca* = 0.2 and *h/a* = 1.5. The inset shows the same scaling with *βDe*. (*b*) Lateral migration velocities, inclination and deformation plotted for varying L^2 values for *Ca* = 0.2, *De* = 0.75 and *h/a* = 1.5. It also shows drop migrating away from the wall for *Ca* = 0.2, *De* = 1.0 *L* = 20 and h_i/a = 1.2.

and inclination decrease dramatically initially, followed by a saturation effect for larger values of *L*. The deformation initially decreases for extremely small values of *L* and then it increases as *L* is increased. The non-monotonicity of drop deformation with increasing *β* or *De* in a viscoelastic matrix is mimicked by increasing *L*. The same figure also shows snapshots of a deforming drop with a pointed tip closer to the wall. Drops in close proximity to the wall form pointed tips if the viscoelasticity in the suspending fluid is sufficiently high as was also found experimentally by Tretheway & Leal (2001). The stagnation points at the tips of a drop cause polymer chains to be extended, resulting in the appearance of pointed ends. The enhanced curvature at the tips also gives rise to very high local strain rate there pulling the drop interface outward. During simulation, the tip remains extended for some time before it relaxes as the drop moves away from the wall. In strong extensional flows, such a tip or a cusp can form, as is seen for a rising bubble or a falling drop in a non-Newtonian media (Philippoff 1937; Pillapakkam *et al.* 2007).

4.3. *Effects of capillary number on quasi-steady dynamics*

Figure 7(*a*) plots the migration velocity against *Ca* for different *De* values and shows that similar to the Newtonian case, the migration velocity here also increases linearly with increasing *Ca*. Increasing *Ca* gives rise to a linear increase in deformation for small deformation. Increased deformation gives rise to increasing migration velocity (see (4.1)). The curves for each *De* is extrapolated to *Ca* = 0. The migration velocity (intercept at the ordinate axis) at *Ca* = 0 plotted in the inset shows a linear variation with *De* (The Newtonian case (*De* = 0) shows a small non-zero migration velocity due to the finite amount of inertia in the simulation). The result indicates a viscoelastic effect even in absence of deformation (see the second term independent of *Ca* in (4.24) below).

As we noted above, there are two distinct but competing effects on migration due to matrix viscoelasticity: the reduced inclination angle and the larger viscoelastic stresses on the curved streamlines above the drop. We will see below in §4.4 that the
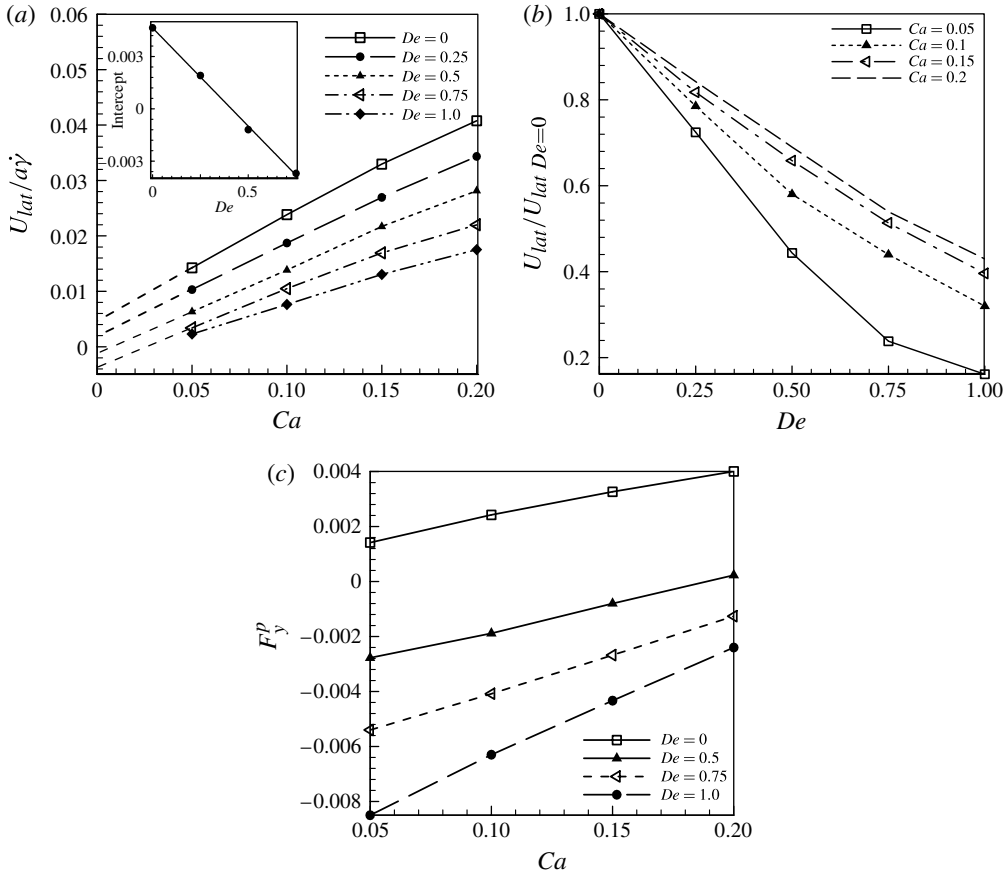
FIGURE 7. (*a*) Lateral migration velocity as a function of *Ca* for varying *De* at $h/a = 1.5$. The inset shows the intercept of the curves on the *y*-axis (when $Ca = 0$). (*b*) Variation of lateral velocities with *De* when the velocities are normalized by the values of the respective Newtonian cases. (*c*) Net vertical viscoelastic force on the drop plotted versus *Ca* for varying *De* at $h/a = 1.5$.

reduced inclination angle increases the lift on the drop while the viscoelastic stresses reduce it. We plot the migration velocity normalized by its Newtonian velocity versus *De* for various *Ca* in figure 7(*b*). It shows that the reduction is larger for smaller capillary numbers. Below (4.22) shows that this results from the normalization with the Newtonian velocity. We also plot the net vertical viscoelastic force exerted by the matrix on the drop as a function of *Ca* (figure 7*c*) for various *De* and for the same instantaneous drop height as in figure 7(*a*). As expected, the higher the Deborah number, the higher the magnitude of the inhibiting (negative) viscoelastic force. With decreasing *Ca*, the magnitude of the negative (retarding) viscoelastic force increases. Also note that for lower *Ca*, the curves for different *De* values are farther apart and as *Ca* increases the curves comes closer to each other, indicating that the effect of viscoelasticity is higher for lower *Ca*. The inclination angle shows a linear decrease with increasing capillary number (not shown here for the reason of brevity).

A moving drop experiences a drag, and as a result moves with a velocity different from that of the imposed flow. The difference is called the slip velocity. Similar to
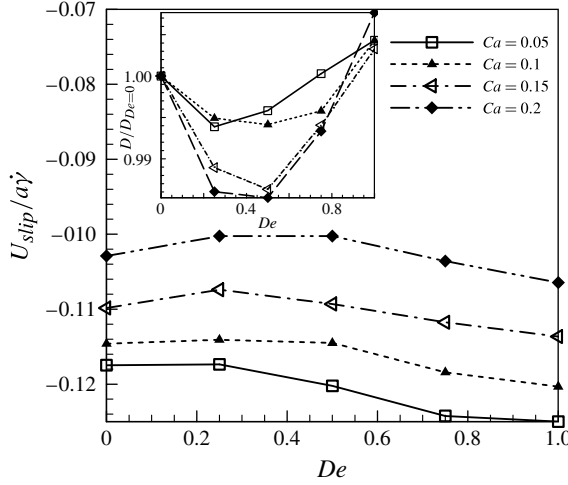
FIGURE 8. Slip velocity plotted against *De* for varying capillary numbers at $h/a = 1.5$. The inset shows normalized deformation versus *De* for the same cases.

the migration velocity, it also decreases linearly with the inverse square of drop-to-wall separation (not shown here for brevity). In figure 8, we plot the dimensionless slip velocity $(U_{slip}/a\dot{\gamma} = (U_x - h\dot{\gamma})/a\dot{\gamma})$ versus *De* at $h/a = 1.5$ for four different *Ca* values. The slip velocity is negative: the drop lags behind the flow. Also the trend is non-monotonic. As *De* is increased, the slip velocity increases slightly, reaches a maximum and then decreases. In the inset, the deformation (normalized with the respective Newtonian value) plotted versus *De* shows a similar trend of non-monotonicity. We conclude that larger deformation results in larger magnitude of the slip velocity.

4.4. *Theory of migration*

In this section, we offer an analytical explanation of the various relations of the quasi-steady migration velocity with the flow parameters, specifically, capillary number, Deborah number and distance from the wall. Note that the only analytical theory available for viscoelastic migration of a drop is due to Chan & Leal (1979), who performed a rigourous perturbative analysis of the moving boundary problem, that is algebraically demanding, and as detailed in the introduction, predicts that viscoelasticity increases migration velocity in contrast to the results shown here and other computations. Here, we take an alternative route to express the solution in terms of integral formulation in terms of Stokes Green's function to find out the first-order variation. Note that in the limit of zero Reynolds number the governing equation can be written as

$$-\nabla\tilde{p} + \mu_d\nabla^2\tilde{\boldsymbol{u}} = 0, \qquad (4.3a)$$

$$-\nabla p + \mu_{sm}\nabla^2\boldsymbol{u} = -\nabla\cdot\boldsymbol{T}^p \quad \text{or} \quad -\nabla p + \mu_m\nabla^2\boldsymbol{u} = -\nabla\cdot(\boldsymbol{T}^p - \mu_{pm}\boldsymbol{D}) = -\nabla\cdot\boldsymbol{T}^{NN}, \qquad (4.3b)$$

inside and outside the drop. Variables with a tilde represent field variables inside the drop. Here, we combine $\mu_{pm}\boldsymbol{D}$ with the viscous part and subtract it from the extra stress. Note that this formulation (4.3) is equivalent to the single-fluid formulation (2.1) adopted earlier for front tracking implementation in the Stokes limit. The

redefined non-Newtonian stress $\boldsymbol{T}^{NN} = \boldsymbol{T}^p - \mu_{pm}\boldsymbol{D}$ gives rise to a force term to the Stokes equation and, therefore, the solution outside the drop can be written as

$$u_j(\boldsymbol{x}) = -\frac{1}{8\pi\mu_m} \int_{A_d+S_\infty} [T_{ik}^v(\boldsymbol{y}) + \mu_{pm}D_{ik}(\boldsymbol{y})]n_k(\boldsymbol{y})G_{ij}(\boldsymbol{x}, \boldsymbol{y}) \, \mathrm{d}A(\boldsymbol{y})$$

$$+ \frac{1}{8\pi} \int_{A_d+S_\infty} u_i(\boldsymbol{y})M_{ijk}(\boldsymbol{x}, \boldsymbol{y})n_k(\boldsymbol{y}) \, \mathrm{d}A(\boldsymbol{y})$$

$$+ \frac{1}{8\pi\mu_m} \int_V \partial_k T_{ik}^{NN}(\boldsymbol{y})G_{ij}(\boldsymbol{x}, \boldsymbol{y}) \, \mathrm{d}A(\boldsymbol{y}), \tag{4.4a}$$

$$G_{ij}(\boldsymbol{x}, \boldsymbol{y}) = G_{ij}^{FS}(\boldsymbol{x}, \boldsymbol{y}) + G_{ij}^w(\boldsymbol{x}, \boldsymbol{y}), \quad M_{ijk}(\boldsymbol{x}, \boldsymbol{y}) = M_{ijk}^{FS}(\boldsymbol{x}, \boldsymbol{y}) + M_{ijk}^w(\boldsymbol{x}, \boldsymbol{y}). \tag{4.4b}$$

Here V is the volume described by the boundary at infinity S_∞ and the wall and the drop surface A_d. We use $\boldsymbol{T}^v$ to denote the viscous stress that only includes the contribution due to solvent viscosity μ_{sm} (2.3). We use a proper Green's function that adds a contribution $G_{ij}^w(\boldsymbol{x}, \boldsymbol{y})$ to the free space Green's function $G_{ij}^{FS}(\boldsymbol{x}, \boldsymbol{y})$ so that $G_{ij}(\boldsymbol{x}, \boldsymbol{y}) = 0$ on the wall (Blake 1971). Here $M_{ijk}(\boldsymbol{x}, \boldsymbol{y})$ is the stress due to this Green's function. This special property of the Green's function along with the no-slip condition eliminates the surface integral over the wall. An integration by parts on the volume integral term gives rise to

$$u_j(\boldsymbol{x}) = -\frac{1}{8\pi\mu_m} \int_{A_d+S_\infty} f_i(\boldsymbol{y})G_{ij}(\boldsymbol{x}, \boldsymbol{y}) \, \mathrm{d}A(\boldsymbol{y}) + \frac{1}{8\pi} \int_{A_d+S_\infty} u_i(\boldsymbol{y})M_{ijk}(\boldsymbol{x}, \boldsymbol{y})n_k(\boldsymbol{y}) \, \mathrm{d}A(\boldsymbol{y})$$

$$- \frac{1}{8\pi\mu_m} \int_V T_{ik}^{NN}(\boldsymbol{y})\partial_k G_{ij}(\boldsymbol{x}, \boldsymbol{y}) \, \mathrm{d}V(\boldsymbol{y}). \tag{4.5}$$

Here $f_i = (T_{ij}^v + \mu_{pm}D_{ij} + T_{ij}^{NN})n_j$ is the total traction at the surface. However, we also know that in the absence of the drop the plane shear indicated as $u_i^\infty = \dot{\gamma}\delta_{i1}x_2$ (direction 2 is in the gradient direction y) is a solution of both viscous as well as viscoelastic momentum equation:

$$\nabla \cdot \boldsymbol{T}^{v(\infty)} = \nabla \cdot \boldsymbol{T}^{NN(\infty)} = 0. \tag{4.6}$$

Therefore, one can write a similar equation such as (4.5) for u_i^∞ in the complete domain without the drop:

$$u_j^\infty(\boldsymbol{x}) = -\frac{1}{8\pi\mu_m} \int_{S_\infty} f_i^\infty(\boldsymbol{y})G_{ij}(\boldsymbol{x}, \boldsymbol{y}) \, \mathrm{d}A(\boldsymbol{y}) + \frac{1}{8\pi} \int_{S_\infty} u_i^\infty(\boldsymbol{y})M_{ijk}(\boldsymbol{x}, \boldsymbol{y})n_k(\boldsymbol{y}) \, \mathrm{d}A(\boldsymbol{y}). \tag{4.7}$$

Note the absence of the volume source term because of (4.6). We write the total velocity as a sum of the imposed shear u_i^∞ and the disturbance velocity u_i' due to the presence of the drop:

$$u_i = u_i^\infty + u_i'. \tag{4.8}$$

Using (4.7) and noting that the disturbance velocity due to the drop vanishes far away, one obtains the velocity field in (4.5) as

$$u_j(\boldsymbol{x}) = u_j^\infty - \frac{1}{8\pi\mu_m} \int_{A_d} f_i(\boldsymbol{y})G_{ij}(\boldsymbol{x}, \boldsymbol{y}) \, \mathrm{d}A(\boldsymbol{y}) + \frac{1}{8\pi} \int_{A_d} u_i(\boldsymbol{y})M_{ijk}(\boldsymbol{x}, \boldsymbol{y})n_k(\boldsymbol{y}) \, \mathrm{d}A(\boldsymbol{y})$$

$$- \frac{1}{8\pi\mu_m} \int_V T_{ik}^{NN}(\boldsymbol{y})\partial_k G_{ij}(\boldsymbol{x}, \boldsymbol{y}) \, \mathrm{d}V(\boldsymbol{y}). \tag{4.9}$$

Using a Green's function formulation for the velocity field $\tilde{u}_j$ inside the drop (normal are opposite to the outside field) but evaluating at a point $\boldsymbol{x}$ outside the drop we obtain

$$0 = \frac{1}{8\pi\mu_d} \int_{A_d} \tilde{f}_i(\boldsymbol{y}) G_{ij}(\boldsymbol{x}, \boldsymbol{y}) \, \mathrm{d}A(\boldsymbol{y}) - \frac{1}{8\pi} \int_{A_d} \tilde{u}_i(\boldsymbol{y}) M_{ijk}(\boldsymbol{x}, \boldsymbol{y}) n_k(\boldsymbol{y}) \, \mathrm{d}A(\boldsymbol{y}). \quad (4.10)$$

Multiplying (4.10) with μ_d/μ_m and adding to (4.9), one obtains

$$u_j(\boldsymbol{x}) = u_j^\infty - \frac{1}{8\pi\mu_m} \int_{A_d} \Delta f_i(\boldsymbol{y}) G_{ij}(\boldsymbol{x}, \boldsymbol{y}) \, \mathrm{d}A(\boldsymbol{y}) + \frac{(1-\lambda_\mu)}{8\pi} \int_{A_d} u_i(\boldsymbol{y}) M_{ijk}(\boldsymbol{x}, \boldsymbol{y}) n_k(\boldsymbol{y}) \, \mathrm{d}A(\boldsymbol{y})$$

$$- \frac{1}{8\pi\mu_m} \int_V T_{ik}^{NN}(\boldsymbol{y}) \partial_k G_{ij}(\boldsymbol{x}, \boldsymbol{y}) \, \mathrm{d}V(\boldsymbol{y}), \quad (4.11)$$

using velocity continuity and traction condition at the drop interface

$$u_i = \tilde{u}_i, \quad f_i - \tilde{f}_i \triangleq \Delta f = \Gamma(\boldsymbol{\nabla} \cdot \boldsymbol{n}) \boldsymbol{n} \quad \text{on } A^d. \quad (4.12)$$

We find an expression appropriate for the far-field by performing a Taylor series around the centre of the drop $\boldsymbol{y}_c$:

$$G_{ij}(\boldsymbol{x}, \boldsymbol{y}) = G_{ij}(\boldsymbol{x}, \boldsymbol{y}_c) + \frac{\partial G_{ij}(\boldsymbol{x}, \boldsymbol{y}_c)}{\partial y_{ck}} (y_k - y_{ck}) + O\left(\frac{a}{|\boldsymbol{y} - \boldsymbol{y}_c|}\right)^3, \quad (4.13a)$$

$$M_{ijk}(\boldsymbol{x}, \boldsymbol{y}) = M_{ijk}(\boldsymbol{x}, \boldsymbol{y}_c) + O\left(\frac{a}{|\boldsymbol{y} - \boldsymbol{y}_c|}\right)^3. \quad (4.13b)$$

We note that although the source term in (4.4) involves an integral of the viscoelastic stresses $\partial_k T_{ik}^{NN} = \partial_k T_{ik}^{NN(\infty)} + \partial_k T_{ik}^{NN'}$ in the whole domain, only $\partial_k T_{ik}^{NN'}$ due to the disturbance field remains (note $\partial_k T_{ik}^{NN(\infty)} = 0$), which is dominant only in a region near the drop. We can therefore use a Taylor series expression even for this term, and obtain

$$u_j(\boldsymbol{x}) = u_j^\infty(\boldsymbol{x}) - \frac{1}{8\pi\mu_m} G_{ij}(\boldsymbol{x}, \boldsymbol{y}_c) \int_{A_d} \Delta f_i(\boldsymbol{y}) \, \mathrm{d}A(\boldsymbol{y})$$

$$- \frac{1}{8\pi\mu_m} \frac{\partial G_{ij}(\boldsymbol{x}, \boldsymbol{y}_c)}{\partial y_{ck}} \left[\int_{A_d} \{\Delta f_i(\boldsymbol{y})(y_k - y_{ck}) - \mu_m (1 - \lambda_\mu)(u_i n_k + u_k n_i)(\boldsymbol{y}) \, \mathrm{d}A(\boldsymbol{y})\} \right.$$

$$\left. + \int_V T_{ik}^{NN'}(\boldsymbol{y}) \, \mathrm{d}V(\boldsymbol{y}) \right], \quad (4.14)$$

noting that $\int_{A_d} u_k(\boldsymbol{y}) n_k(\boldsymbol{y}) \, \mathrm{d}A(\boldsymbol{y}) = 0$ (this eliminates the pressure and the transpose part in $M_{ijk}(\boldsymbol{x}, \boldsymbol{y}_c)$). For a force-free drop, $\int_{A_d} \Delta f_j(\boldsymbol{y}) \, \mathrm{d}A(\boldsymbol{y}) = 0$. We obtain the stresslet expression due to the drop

$$u_j(\boldsymbol{x}) = u_j^\infty(\boldsymbol{x}) - \frac{1}{8\pi\mu_m} \frac{\partial G_{ij}(\boldsymbol{x}, \boldsymbol{y}_c)}{\partial y_{ck}}$$

$$\times \left\{ \Gamma \int_{A_d} (\delta_{ik} - n_i n_k) \, \mathrm{d}A(\boldsymbol{y}) - \mu_m (1 - \lambda_\mu) \int_{A_d} (u_i n_k + u_k n_i)(\boldsymbol{y}) \, \mathrm{d}A(\boldsymbol{y}) \right.$$

$$\left. + \int_V T_{ik}^{NN'}(\boldsymbol{y}) \, \mathrm{d}V(\boldsymbol{y}) \right\}$$

$$= u_j^\infty(\boldsymbol{x}) - \frac{1}{8\pi\mu_m} \frac{\partial G_{ij}(\boldsymbol{x}, \boldsymbol{y}_c)}{\partial y_{ck}} \left(S_{ik}^{int'} + S_{ik}^{vrat'} + S_{ik}^{NN'} \right)$$

$$= u_j^\infty(\boldsymbol{x}) - \frac{1}{8\pi\mu_m} \frac{\partial G_{ij}(\boldsymbol{x}, \boldsymbol{y}_c)}{\partial y_{ck}} \left(S_{ik}^{int} + S_{ik}^{vrat} + S_{ik}^{NN} \right), \tag{4.15}$$

where

$$S_{ik}^{int'} = \Gamma \int (\delta_{ik} - n_i n_k) \, \mathrm{d}A(\boldsymbol{y}), \tag{4.16a}$$

$$S_{ik}^{vrat'} = -\mu_m \left(1 - \lambda_\mu\right) \int_{A_d} (u_i n_k + u_k n_i)(\boldsymbol{y}) \, \mathrm{d}A(\boldsymbol{y}), \tag{4.16b}$$

$$S_{ik}^{NN'} = \int_V T_{ik}^{NN'}(\boldsymbol{y}) \, \mathrm{d}V(\boldsymbol{y}), \tag{4.16c}$$

are the contributions to the stresslet due to the interfacial tension, viscosity ratio and the non-Newtonian effects. These terms without primes in the last expression in (4.15) represent their traceless forms. Note that due to incompressibility, $\partial G_{ik}(\boldsymbol{x}, \boldsymbol{y}_c)/\partial y_{ck} = 0$. Therefore, the trace of the stresslets does not contribute. In arriving at (4.15), we used an identity due to Rosenkilde (1967) to transform the surface integral term involving curvature due to interfacial tension for S_{ik}^{int} to the interface tensor $\int (\delta_{ik} - n_i n_k) \, \mathrm{d}A(\boldsymbol{y})$ first so defined by Batchelor (1970). The first two terms are responsible for migration as well as effective emulsion rheology (Li & Sarkar 2005b; Singh & Sarkar 2011) in a Newtonian system. Note that this term is entirely geometric determined by the drop shape.

The drop migration, as noted by Smart & Leighton (1991) for a viscous system, is caused by the velocity field due to the image of the stresslet due to the wall, i.e. the contribution due to $G_{ij}^w(\boldsymbol{x}, \boldsymbol{y})$ in relation (4.4) towards $\partial G_{ij}(\boldsymbol{x}, \boldsymbol{y}_c)/\partial y_{ck}$ in (4.15). Smart and Leighton obtained that near a rigid wall with normal $\boldsymbol{n}$, expression (4.15) gives rise to the following drift velocity (contribution due to the image):

$$u_j^{drift} n_j = -\frac{1}{8\pi\mu_m} \left(\frac{9}{8h^2} \right) \left(S_{ik}^{int} + S_{ik}^{vrat} + S_{ik}^{NN} \right) n_i n_k, \quad \left(\frac{a}{h} \right)^2 \ll 1. \tag{4.17}$$

For the case here with the wall at $x_2 = y = 0$, we obtain the migration velocity

$$U_{lat} = -\frac{1}{8\pi\mu_m} \left(\frac{9}{8h^2} \right) \left(S_{22}^{int} + S_{22}^{vrat} + S_{22}^{NN} \right). \tag{4.18}$$

The second term is absent for a viscosity matched system ($\lambda_\mu = 1$). For such a case, figure 9(a) examines the validity of the expression (4.18) for a Newtonian system where only S_{22}^{int} survives. The simulated migration velocity is compared with that obtained from (4.18) using S_{22}^{int} computed from the simulated drop shape for several Ca values. The comparison is similar to what was obtained with the formula due to Chan & Leal (1979); it is good for drops away from the wall. We therefore choose a distance of $h = 2.5a$ where Newtonian comparison works well for examining the effects of the viscoelasticity.

We note that in a sheared FENE-CR liquid, the imposed shear obtains only one component of the normal non-Newtonian stress (Oliveira 2003)

$$T_{11}^{NN(\infty)} = (\mu_p/2\lambda) \left[-L^2 + \sqrt{L^4 + 8\lambda^2 \dot{\gamma}^2 (L^2 - 3)} \right]. \tag{4.19}$$

We subtract it from the total normal non-Newtonian stress T_{11}^{NN} to obtain the normal stress due to the perturbation field. Also note that accounting for the trace, the non-
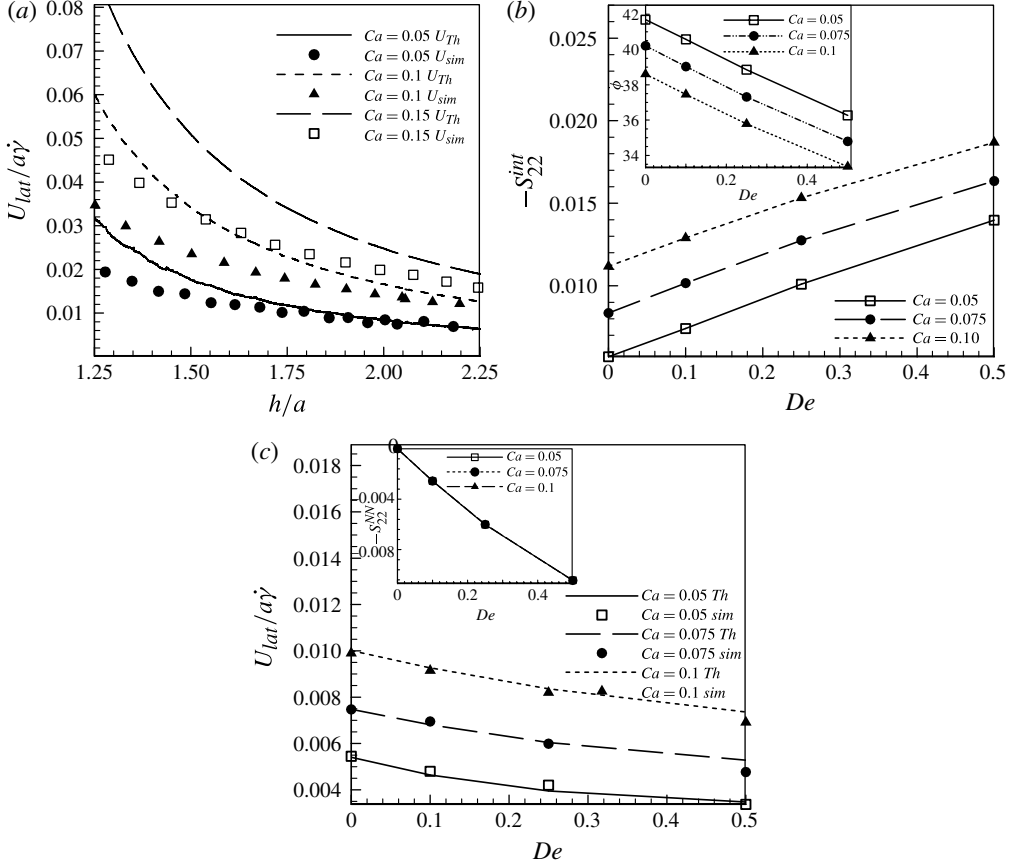
FIGURE 9. (*a*) Lateral migration velocity from the simulations (symbols) and from the stresslet theory (lines) are shown for Newtonian cases for three sets of *Ca*. (*b*) Interfacial part of stresslet is plotted as a function of *De* for different *Ca* values at $h/a = 2.5$. Inset shows the inclination angle for same parameters. (*c*) Migration velocity according to the stresslet theory (lines) are compared with those from the simulations (symbols) for varying *De* and three *Ca* values. Inset shows the non-Newtonian part of the stresslet.

Newtonian stresslet contribution becomes

$$S_{22}^{NN} = \int_V \left(T_{22}^{NN'} - \frac{T_{22}^{NN'} + T_{11}^{NN'} + T_{33}^{NN'}}{3} \right) dV = \int_V \left(\frac{N_1^{NN'} - N_2^{NN'}}{3} \right) dV. \quad (4.20)$$

Ma & Graham (2005) also found a linear relationship between the shear-induced migration velocity near a wall in a dilute polymer solution and the $(N_1 - N_2)$ of the solution. The system of dilute polymer solution that was simulated using a bead-spring dumbbell model for polymer chains is different, yet bears similarity: the beads joined by the spring experiences equal but opposite forces giving rise to a stresslet. The authors provided a theory that clearly demonstrated that the polymer depletion layer near a wall is primarily caused by the inter-molecular hydrodynamic interactions.

We have noted in previous subsections that increasing viscoelasticity decreases the inclination angle aligning the drop with the flow (figure 3*b*), while the drop migration decreases (figure 4*c*) both linearly with viscoelasticity parameter βDe. Evidently,

decreasing the inclination angle affects the geometric term S_{22}^{int}. One would be inclined to think that decreasing the angle restores the symmetry of the system containing the drop in vicinity of the wall and therefore the migration velocity induced by the geometric stresslet S_{22}^{int} would decrease. However, figure 9(b) shows that S_{22}^{int} increases linearly with *De* for several *Ca*, at $h = 2.5a$, indicating that it tends to increase the migration velocity, while, counter to one's intuition, the inclination angle (shown in the inset) linearly decreases. In fact, they are closely related; empirically we find from simulation

$$\phi = \pi/4 - 1.134\,[Ca + 0.37(\beta De) - 0.375(Ca\beta De)] \qquad (4.21a)$$

$$-S_{22}^{int} = 0.114\,[Ca + 0.34(\beta De) - 0.875(Ca\beta De)]\,. \qquad (4.21b)$$

The second term involving βDe in $-S_{22}^{int}$ increases migration velocity. But it is compensated by the non-Newtonian stresslet contribution $-S_{22}^{NN}$. Shown in the inset of figure 9(c) for the same parameters as in figure 9(b), $-S_{22}^{NN}$ computed using simulated viscoelastic stresses decreases with *De* as

$$-S_{22}^{NN} \approx -0.054\beta De + 0.048(\beta De)^2. \qquad (4.22)$$

Note that curves for different *Ca* nearly coincides indicating very little effect of capillary number for S_{22}^{NN}. In figure 9(c), simulated migration velocity shows good match with those from the theoretical expression (4.18) (stresslets are computed using shapes and viscoelastic stresses from simulation) for moderate values of *De*. Note that the first term in (4.22), which decreases migration velocity with increasing βDe, explains the relatively pronounced effect of viscoelasticity seen for smaller capillary number when normalized with Newtonian velocity (figure 7b). In view of the above, we further reiterate that the effects of matrix viscoelasticity on drop migration is a result of two competing effects: decreased inclination angle (increased alignment with the flow) due to viscoelasticity tries to increase lateral migration, but the viscoelastic normal stresses overcomes it resulting in a hindered migration.

4.5. *An expression for the quasi-steady migration velocity*

We develop a correlation for the lateral migration in a viscoelastic medium based on our observation and the analysis of the stresslet sketched in the previous subsection. We noticed that $U_{lat}/a\dot{\gamma}$ decreases linearly with βDe (figure 6a) suggesting $U_{lat} \sim U_{lat(De=0)}(1 - \alpha(\beta De))$, where α is solely a function of *Ca*. The analytical relation (4.1) due to Chan and Leal and the relation $D \sim Ca$ indicate that $U_{lat(De=0)} \sim Ca(a/h)^2$. Therefore, $U_{lat} \sim (a/h)^2 Ca(1 - \alpha(\beta De))$. We also note that for $Ca = 0$, inset of figure 7(a) indicates a contribution linear with viscoelasticity $\sim(\beta De)$ independent of *Ca*. Furthermore the stresslet terms (4.21b) and (4.22) also insinuate such a term. Therefore $\alpha \sim \kappa_1 + \kappa_2/Ca$. Using the simulated data we obtain

$$\frac{U_{lat}}{a\dot{\gamma}} = 0.48\left(\frac{a}{h}\right)^2 Ca \left(1 - 0.665\beta De - 0.1055\frac{\beta De}{Ca}\right). \qquad (4.23)$$

Note that the slope 0.48 is lower than the values 0.6 obtained by Chan & Leal (1979) and 0.583 obtained by Smart & Leighton (1991) consistent with the figure 2(a), where the migration velocity obtained by Chan and Leal overpredicts the simulated migration velocity. On the other hand, from the curves obtained using BEM simulation of Uijttewaal *et al.* (1993), we estimate a value in the range 0.44–0.49. Imaeda (2000) used a different perturbative method (using Green's function formulation and expanding the interface shape over spherical harmonics) to obtain a value of 0.41.
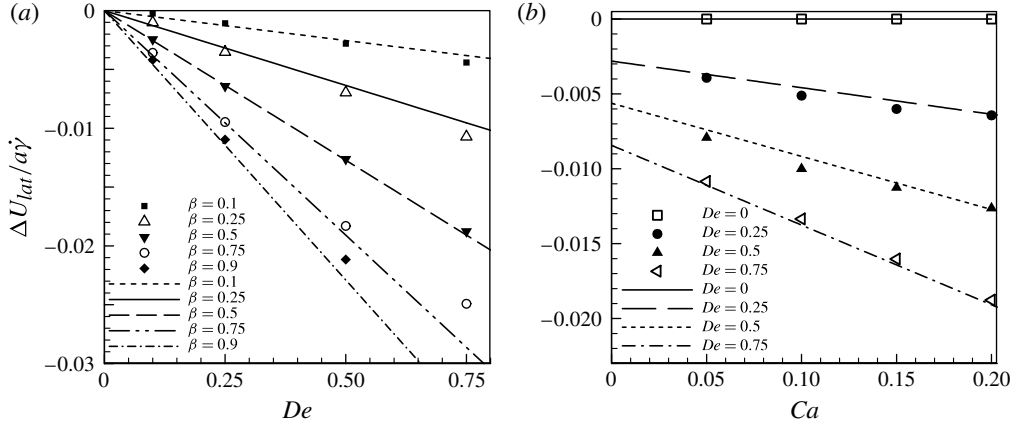
FIGURE 10. Empirical expression (4.24) based on the simulation is plotted (lines) with the simulation data (symbols). Change in lateral migration velocity with varying (*a*) *De* for various *β* and (*b*) capillary number for various *De* at $h/a = 1.5$.

Note that the value here is close to that obtained using BEM solution, as was also the case in figure 2(*a*). Owing to the small but finite inertia effects in our simulation, it is more appropriate to compare the change in migration velocity due to matrix viscoelasticity

$$\frac{\Delta U_{lat}}{a\dot{\gamma}} \equiv \frac{U_{lat} - U_{lat(De=0)}}{a\dot{\gamma}} = -0.48\left(\frac{a}{h}\right)^2 (0.665(Ca\beta De) + 0.1055(\beta De)). \quad (4.24)$$

Figure 10(*a*) plots this relation against *De* for five sets of *β* values along with the simulated data, while figure 10(*b*) shows variation with *Ca* for various *De* values. Both figures show good match for low to moderate values of Deborah number. For higher values of *βDe*, there is a difference because of higher-order contributions of the order $(\beta De)^2$.

4.6. *Transient effects*

Above, we investigated migration when the drop reaches a quasi-steady dynamics. The migrating drop however deforms from its initial shape through a transient phase. Viscoelasticity adds to the transients because the viscoelastic stresses unlike viscous stresses take finite time to grow. Figure 11(*a*) plots the migration velocity for $De = 0$ and 0.75 for two different initial heights and $Ca = 0.2$. As expected, the initial rise in velocity is higher for a drop initially closer to the wall due to enhanced wall-induced asymmetry. By plotting the change in velocity normalized by the maximum change (inset of figure 11*a*), one sees that the curves for different initial drop distance from the wall collapse onto a single curve, indicating that the time scale of growth is a function only of the Deborah number.

As noted above, once the moving drop becomes quasi-steady, the change in the slip velocity due to viscoelasticity is minimal for $Ca = 0.2$. However, figure 11(*b*) shows that for the same initial height, drop in the viscoelastic matrix ($De = 0.75$) experiences an overshoot in slip velocity which crosses the Newtonian value for a period of time. For the same Deborah number, a drop further away from the wall has a slightly higher slip velocity. When the velocity change is normalized by the maximum change, once again curves belonging to the same Deborah number collapse onto each other
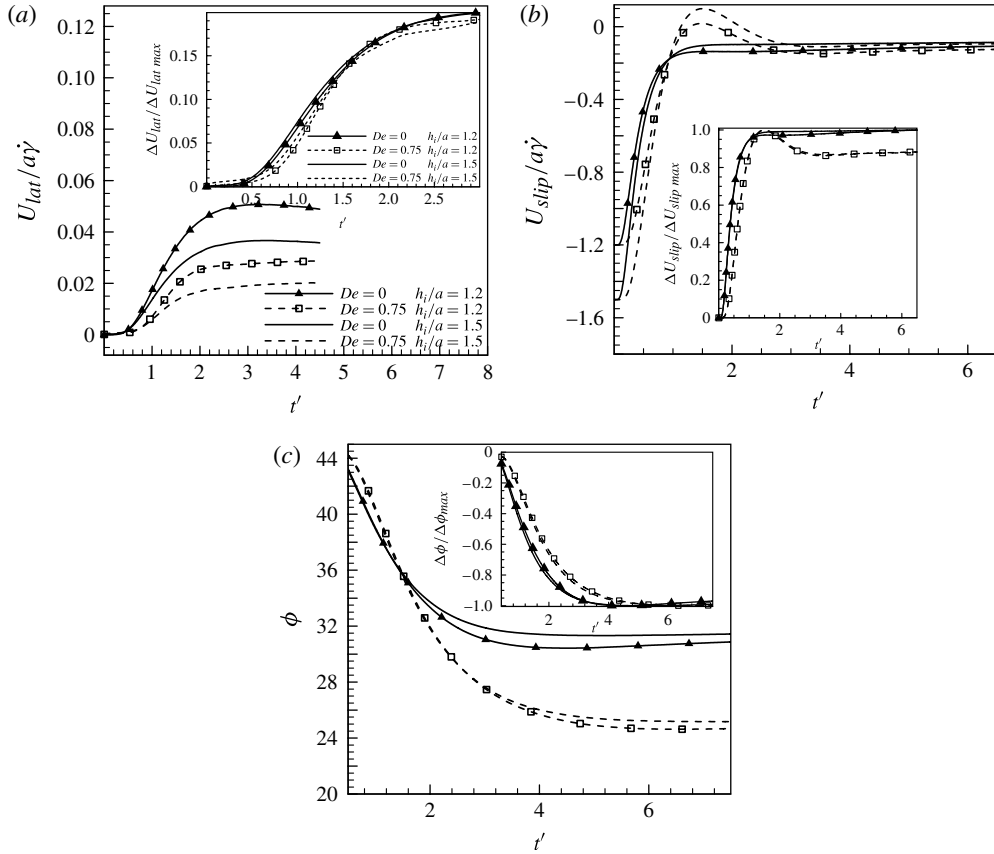
FIGURE 11. Transient evolution of (*a*) migration velocity, (*b*) slip velocity and (*c*) orientation angle for $Ca = 0.2$ for two different initial heights. The insets show the change in same quantities relative to the Newtonian case normalized by the corresponding maximum value during the transient.

irrespective of the starting position (inset). The same is true for the inclination angle as well (figure 11*c*), as one would expect from the close relationship between the inclination and the viscoelastic effects on drop motion.

4.7. *Large deformation and breakup*

So far, we have studied cases where deformation is relatively moderate ($Ca \leqslant 0.2$) and the drop remains bounded. For these cases, the drop eventually reaches a quasi-steady state independent of the history and the initial drop–wall separation, and only depends on the instantaneous separation from the wall. More specifically, the quasi-steady lateral velocity varies linear with $(a/h)^2$. In this section, we very briefly investigate cases where the drop experiences large deformation. In figure 12, we investigate the Newtonian case ($De = 0$) by plotting the lateral velocity against h/a for $Ca = 0.4$ and three different initial drop heights. For such large Ca values and consequently large deformation, the migration velocity does not become independent of the initial drop height; a drop which starts closer to the wall has a larger maximum velocity. Initially, the velocity rises rapidly, similar to the lower Ca cases, as the drop deforms from its spherical shape. But after this initial period, velocity does not bear the $(a/h)^2$ scaling;
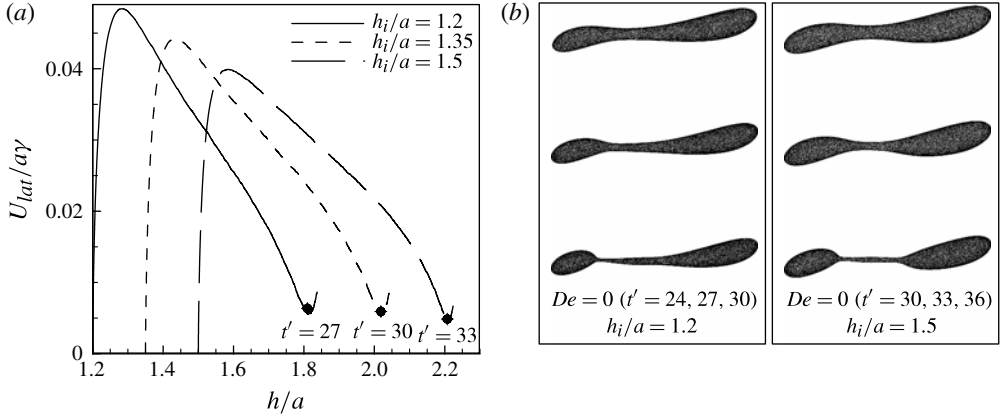
FIGURE 12. (*a*) Viscous drop in a Newtonian matrix: (*a*) migration velocities are plotted against wall distances for three different initial drop heights for the same $Ca = 0.4$. (*b*) Drop shapes are shown at three time instances for two sets of initial drop height. The shapes are shown before, at and after the time marked in (*a*).

it decreases almost linearly with distance from the wall (figure 12*a*). The drop which attains higher velocity in the initial period has a quicker decay afterwards. The drop shapes shown for three consecutive time instants and $h_i/a = 1.2$ and $h_i/a = 1.5$ in figure 12(*b*) indicate that the drops stretch and experience necking initiating breakup. The migration velocity (computed for the centre of mass) tends to increase post-necking; time instants for necking are indicated in the velocity plots. The drop becomes more like two satellite daughter droplets, ellipsoidal in shape, attached by a cylindrical thread. The increase in migration velocity post-necking might be ascribed to this change in shape from a cylindrical shape to such a double-ellipsoidal shapes. The daughter droplet that would be generated close to the wall is smaller than the other one. The breakup process takes a long time and we have stopped our simulations when the neck has become less than 4 % of the initial radius.

   Next we consider a drop with the same capillary number $Ca = 0.4$ in a viscoelastic matrix. Effects of matrix viscoelasticity on the drop breakup was seen to be non-monotonic by Aggarwal & Sarkar (2008*a*). For a drop experiencing breakup in a Newtonian matrix, introduction of matrix viscoelasticity first leads to a bounded shape due to decreased inclination away from the extensional axis of the shear (at 45°), but further increase results in increased deformation and possible breakup due to large viscoelastic stresses at the tips. Here, we note similar effects in the presence of wall effects and migration. The extensibility of FENE for these cases is reduced to $L^2 = 200$ to preclude drop shapes with highly stretched tips. In figure 13(*a*), we plot the length of the semi-major axis of the migrating drop for several Deborah numbers for $h_i/a = 1.5$. The Newtonian drop breaks (figure 12). But introducing viscoelasticity stabilizes the drop: initially it grows to a maximum size but then relaxes to a stable shape. This inhibition of breakup is because of the decreased viscous stretching due to reduced drop inclination. Figure 13(*b*) shows the migration velocity for the same set of parameters; viscoelastic stabilization reduces the drop velocity gradually. The inset of figure 13(*b*) shows typical stabilized drop shapes which are different from those seen in Newtonian matrix. Figure 13(*c,d*) plots the same cases but for $h_i/a = 1.2$. Here, for all of the Deborah numbers considered, the drop undergoes breakup due
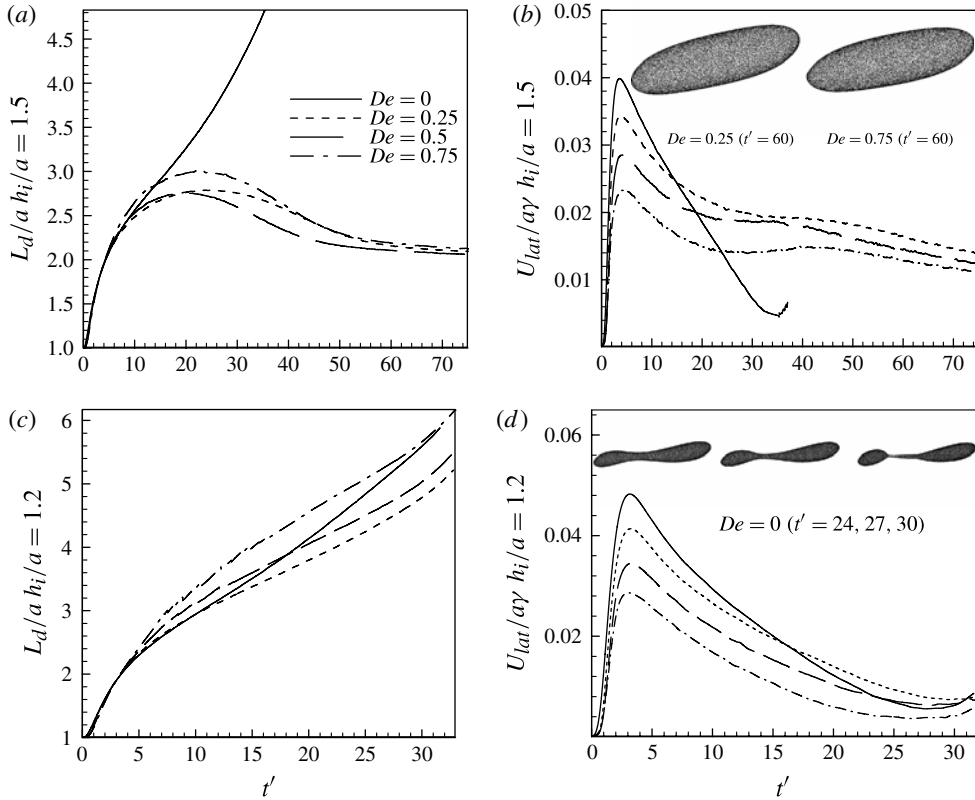
FIGURE 13. The dimensionless length of the semi-major axis of the drop (*a*) and the migration velocity (*b*) for $h_i/a = 1.5$ and $Ca = 0.4$. The inset of (*b*) shows drop shapes for $De = 0.25$ and 0.75 at a non-dimensional time of 60. The dimensionless length of the semi-major axis of the drop (*c*) and the migration velocity (*d*) for $h_i/a = 1.2$ and $Ca = 0.4$. The inset of (*d*) shows drop shapes for $De = 0.5$ for three time instances (before, at and after the minimum velocity is achieved).

to the increased viscous and viscoelastic stresses in the proximity of the wall. They experience an increase in migration velocity after necking similar to the viscous case. To delineate the details of this time-dependent dynamics, a far more comprehensive parametric study is needed, not pursued here for the reason of brevity. We merely conclude that unlike the cases with moderate deformation, the dynamics here is no more independent of the initial drop height. The change in initial drop height can lead to very different dynamics: from bounded drop to drop breakup.

5. Conclusion

We have numerically simulated the effects of matrix viscoelasticity on the migration of a deforming drop suspended in a shear flow near a wall. The matrix viscoelasticity is modelled using FENE–CR constitutive equation. For Newtonian cases, simulated migration velocity and the excess deformation match well with previous analytical results (Chan & Leal 1979; Shapira & Haber 1990) and BEM simulations (Uijttewaal *et al.* 1993). Adding viscoelasticity in the matrix retards the migration process. Similar to the Newtonian case, after an initial transient period, the drop reaches a quasi-steady

case, when the migration velocity for low Deborah numbers depends only on the instantaneous drop position and scales linearly with inverse of the square of drop–wall separation. The velocity varies linearly with viscoelasticity βDe. The local extensional flow near the tips gives rise to large viscoelastic stresses for high De, particularly at the tip near the wall leading to highly stretched drop tip. The tip becomes smoother as the drop moves away from the wall.

Viscoelasticity reduces drop inclination, and deformation varies non-monotonically. The decreasing drop inclination tries to increase migration. However, it is overcome by the viscoelastic tensile force along the streamline around the drop resulting in retarded migration compared with the Newtonian case. The slip velocity varies non-monotonically with increasing viscoelasticity in a similar fashion as that of the deformation. During the transient part of the migration, the response time scale of the velocity and the inclination growth is dependent only on the Deborah number.

The perturbative theory relating the stresslet, the non-Newtonian stress and the lateral migration velocity clearly demonstrates the underlying physics. One would expect that decreasing drop inclination (alignment with the flow) restores fore–aft drop symmetry, and therefore is responsible for decreased lateral migration. However, the stresslet theory shows that the decreasing inclination angle counter-intuitively increases the interfacial stresslet contribution aiding drop migration. The decreased migration is due to the larger retarding effect of the non-Newtonian contribution to the stresslet (the difference of first and second normal non-Newtonian stresses). Using the simulation and the theory, we obtain an algebraic expression for the migration velocity as a function of Ca, De and β.

We briefly consider a case of larger capillary number ($Ca = 0.4$) to show that the larger deformation prevents attainment of a quasi-steady state: the drop dynamics depends on initial drop heights. For the Newtonian case, for this capillary number, the drop eventually breaks by a necking process. The migration velocity initially decreases linearly with drop height. However, after initiation of the necking process, the migration velocity tends to increase. Introduction of matrix viscoelasticity tends to stabilize the drop against breakup: it renders bounded drops that are initially at larger heights away from the wall, but fails to prevent breakup for those initially closer to the wall, details depending on the many parameters of the problem. For larger deformation, the drop dynamics for both Newtonian and viscoelastic cases remain dependent on the initial condition.

Acknowledgements

REFERENCES

AGGARWAL, N. & SARKAR, K. 2007 Deformation and breakup of a viscoelastic drop in a Newtonian matrix under steady shear. *J. Fluid Mech.* **584**, 1–21.

AGGARWAL, N. & SARKAR, K. 2008*a* Effects of matrix viscoelasticity on viscous and viscoelastic drop deformation in a shear flow. *J. Fluid Mech.* **601**, 63–84.

AGGARWAL, N. & SARKAR, K. 2008*b* Rheology of an emulsion of viscoelastic drops in steady shear. *J. Non-Newtonian Fluid Mech.* **150**, 19–31.

BARTRAM, E., GOLDSMITH, H. L. & MASON, S. G. 1975 Particle motions in non-newtonian media III. Further observations in elasticoviscous fluids. *Rheol. Acta* **14**, 776–782.

BATCHELOR, G. K. 1970 Stress system in a suspension of force-free particles. *J. Fluid Mech.* **41**, 545–570.

BLAKE, J. R. 1971 A note on the image system for a stokeslet in a no-slip boundary. *Proc. Camb. Phil. Soc. Math. Phys. Sci.* **70**, 303–310.

BRETHERTON, F. P. 1962 The motion of rigid particles in a shear flow at low Reynolds number. *J. Fluid Mech.* **14**, 284–304.

CANTAT, I. & MISBAH, C. 1999 Lift force and dynamical unbinding of adhering vesicles under shear flow. *Phys. Rev. Lett.* **83**, 880–883.

CHAFFEY, C. E., BRENNER, H. & MASON, S. G. 1965 Particle motions in sheared suspensions XVIII: Wall migration. *Rheol. Acta* **4**, 64–72.

CHAN, P. C. H. & LEAL, L. G. 1977 Note on motion of a spherical-particle in a general quadratic flow of a 2nd-order fluid. *J. Fluid Mech.* **82**, 549–559.

CHAN, P. C. H. & LEAL, L. G. 1979 The motion of a deformable drop in a second-order fluid. *J. Fluid Mech.* **92**, 131–170.

CHILCOTT, M. D. & RALLISON, J. M. 1988 Creeping flow of dilute polymer solutions past cylinders and spheres. *J. Non-Newtonian Fluid Mech.* **29**, 381–432.

COATES, P. J., ARMSTRONG, R. C. & BROWN, R. A. 1992 Calculation of steady-state viscoelastic flow through axisymmetric contractions with the EEME formulation. *J. Non-Newtonian Fluid Mech.* **42**, 141–188.

D'AVINO, G., MAFFETTONE, P. L., GRECO, F. & HULSEN, M. A. 2010*a* Viscoelasticity-induced migration of a rigid sphere in confined shear flow. *J. Non-Newtonian Fluid Mech.* **165**, 466–474.

D'AVINO, G., TUCCILLO, T., MAFFETTONE, P. L., GRECO, F. & HULSEN, M. A. 2010*b* Numerical simulations of particle migration in a viscoelastic fluid subjected to shear flow. *Comput. Fluids* **39**, 709–721.

DOU, H.-S. & PHAN-THIEN, N. 2003 Negative wake in the uniform flow past a cylinder. *Rheol. Acta* **42**, 383–409.

ELMENDORP, J. J. & MAALCKE, R. J. 1985 A study on polymer blending microrheology. 1. *Polym. Engng Sci.* **25**, 1041–1047.

FENG, J. & JOSEPH, D. D. 1996 The motion of solid particles suspended in viscoelastic liquids under torsional shear. *J. Fluid Mech.* **324**, 199–222.

FLUMERFELT, R. W. 1972 Drop breakup in simple shear fields of viscoelastic fluids. *Ind. Engng Chem. Fundam.* **11**, 312–318.

GAUTHIER, F., GOLDSMITH, H. L. & MASON, S. G. 1971*a* Particle motions in non-Newtonian media I: Couette flow. *Rheol. Acta* **10**, 344–364.

GAUTHIER, F., GOLDSMITH, H. L. & MASON, S. G. 1971*b* Particle motions in non-Newtonian media. II: Poiseuille flow. *Trans. Soc. Rheol.* **15**, 297–330.

GOLDSMITH, H. L. & MASON, S. G. 1962 Flow of suspensions through tubes. 1. Single spheres, rods, and disks. *J. Colloid Sci.* **17**, 448–476.

HEGLER, R. P. & MENNIG, G. 1985 Phase-separation effects in processing of glass-bead-filled and glass-fiber-filled thermoplastics by injection-molding. *Polym. Engng Sci.* **25**, 395–405.

HO, B. P. & LEAL, L. G. 1976 Migration of rigid spheres in a 2-dimensional unidirectional shear-flow of a 2nd-order fluid. *J. Fluid Mech.* **76**, 783–799.

HUANG, P. Y., FENG, J., HU, H. H. & JOSEPH, D. D. 1997 Direct simulation of the motion of solid particles in Couette and Poiseuille flows of viscoelastic fluids. *J. Fluid Mech.* **343**, 73–94.

IMAEDA, T. 2000 Shear-induced migration of a droplet in the presence of a plane wall. *Physica* A **285**, 306–314.

JEFFERY, G. B. 1922 The motion of ellipsoidal particles immersed in a viscous fluid. *Proc. R. Soc. Lond. Ser.* A **102**, 161–179.

JOSEPH, D. D. & FENG, J. 1996 A note on the forces that move particles in a second-order fluid. *J. Non-Newtonian Fluid Mech.* **64**, 299–302.

KARNIS, A. & MASON, S. G. 1966 Particle motions in sheared suspensions. XIX. Viscoelastic media. *Trans. Soc. Rheol.* **10**, 571–592.

KARNIS, A. & MASON, S. G. 1967 Particle motions in sheared suspensions: XXIII. Wall migration of fluid drops. *J. Colloid Interface Sci.* **24**, 164–169.

KENNEDY, M. R., POZRIKIDIS, C. & SKALAK, R. 1994 Motion and deformation of liquid-drops, and the rheology of dilute emulsions in simple shear-flow. *Comput. Fluids* **23**, 251–278.

KIM, J. M., KIM, C., CHUNG, C., AHN, K. H. & LEE, S. J. 2005 Negative wake generation of FENE-CR fluids in uniform and Poiseuille flows past a cylinder. *Rheol. Acta* **44**, 600–613.

LEAL, L. G. 1979 The motion of small particles in non-Newtonian fluids. *J. Non-Newtonian Fluid Mech.* **5**, 33–78.

LEAL, L. G. 1980 Particle motions in a viscous-fluid. *Annu. Rev. Fluid Mech.* **12**, 435–476.

LEAL, L. G. 2007 *Advanced Transport Phenomena: Fluid Mechanics and Convective Transport*. Cambridge University Press.

LI, X. Y. & SARKAR, K. 2005a Drop dynamics in an oscillating extensional flow at finite Reynolds numbers. *Phys. Fluids* **17**, 027103.

LI, X. Y. & SARKAR, K. 2005b Effects of inertia on the rheology of a dilute emulsion of drops in shear. *J. Rheol.* **49**, 1377–1394.

LI, X. Y. & SARKAR, K. 2005c Numerical investigation of the rheology of a dilute emulsion of drops in an oscillating extensional flow. *J. Non-Newtonian Fluid Mech.* **128**, 71–82.

LI, X. Y. & SARKAR, K. 2006 Drop deformation and breakup in a vortex at finite inertia. *J. Fluid Mech.* **564**, 1–23.

LORMAND, B. M. & PHILLIPS, R. J. 2004 Sphere migration in oscillatory Couette flow of a viscoelastic fluid. *J. Rheol.* **48**, 551–570.

MA, H. B. & GRAHAM, M. D. 2005 Theory of shear-induced migration in dilute polymer solutions near solid boundaries. *Phys. Fluids* **17**, 083103.

MATOS, H. M., ALVES, M. A. & OLIVEIRA, P. J. 2009 New formulation for stress calculation: application to viscoelastic flow in a T-junction. *Numer. Heat Transfer* B **56**, 351–371.

MOYERS-GONZALEZ, M. & FRIGAARD, I. 2010 The critical wall velocity for stabilization of plane Couette–Poiseuille flow of viscoelastic fluids. *J. Non-Newtonian Fluid Mech.* **165**, 441–447.

MUKHERJEE, S. & SARKAR, K. 2009 Effects of viscosity ratio on deformation of a viscoelastic drop in a Newtonian matrix under steady shear. *J. Non-Newtonian Fluid Mech.* **160**, 104–112.

MUKHERJEE, S. & SARKAR, K. 2010 Effects of viscoelasticity on the retraction of a sheared drop. *J. Non-Newtonian Fluid Mech.* **165**, 340–349.

MUKHERJEE, S. & SARKAR, K. 2011 Viscoelastic drop falling through a viscous medium. *Phys. Fluids* **23**, 013101.

OLAPADE, P. J., SINGH, R. K. & SARKAR, K. 2009 Pair-wise interactions between deformable drops in free shear at finite inertia. *Phys. Fluids* **21**, 063302.

OLIVEIRA, P. J. 2003 Asymmetric flows of viscoelastic fluids in symmetric planar expansion geometries. *J. Non-Newtonian Fluid Mech.* **114**, 33–63.

OLIVEIRA, P. J. & MIRANDA, A. L. I. P. 2005 A numerical study of steady and unsteady viscoelastic flow past bounded cylinders. *J. Non-Newtonian Fluid Mech.* **127**, 51–66.

PHILIPPOFF, W. 1937 Viscosity characteristics of rubber solution. *Rubber Chem. Tech.* **10**, 76–106.

PILLAPAKKAM, S. B., SINGH, P., BLACKMORE, D. & AUBRY, N. 2007 Transient and steady state of a rising bubble in a viscoelastic fluid. *J. Fluid Mech.* **589**, 215–252.

RAMASWAMY, S. & LEAL, L. G. 1999 The deformation of a viscoelastic drop subjected to steady uniaxial extensional flow of a Newtonian fluid. *J. Non-Newtonian Fluid Mech.* **85**, 127–163.

ROCHA, G. N., POOLE, R. J. & OLIVEIRA, P. J. 2007 Bifurcation phenomena in viscoelastic flows through a symmetric 1:4 expansion. *J. Non-Newtonian Fluid Mech.* **141**, 1–17.

ROSENKILDE, C. E. 1967 Surface-energy tensors. *J. Math. Phys.* **8**, 84–88.

SAFFMAN, P. G. 1956 On the motion of small spheroidal particles in a viscous liquid. *J. Fluid Mech.* **1**, 540–553.

SAHIN, M. & OWENS, R. G. 2004 On the effects of viscoelasticity on two-dimensional vortex dynamics in the cylinder wake. *J. Non-Newtonian Fluid Mech.* **123**, 121–139.

SARKAR, K. & SCHOWALTER, W. R. 2000 Deformation of a two-dimensional viscoelastic drop at non-zero Reynolds number in time-periodic extensional flows. *J. Non-Newtonian Fluid Mech.* **95**, 315–342.

SARKAR, K. & SCHOWALTER, W. R. 2001 Deformation of a two-dimensional drop at non-zero Reynolds number in time-periodic extensional flows: numerical simulation. *J. Fluid Mech.* **436**, 177–206.

SHAPIRA, M. & HABER, S. 1990 Low Reynolds number motion of a droplet in shear flow including wall effects. *Intl J. Multiphase Flow* **16**, 305–321.

SINGH, R. K. & SARKAR, K. 2011 Inertial effects on the dynamics, streamline topology and interfacial stresses due to a drop in shear. *J. Fluid Mech.* **683**, 149–171.

SMART, J. R. & LEIGHTON, D. T. Jr. 1991 Measurement of the drift of a droplet due to the presence of a plane. *Phys. Fluids* A **3**, 21–28.

SZABO, P., RALLISON, J. M. & HINCH, E. J. 1997 Start-up of flow of a FENE-fluid through a 4:1:4 constriction in a tube. *J. Non-Newtonian Fluid Mech.* **72**, 73–86.

TAVGAC, T. 1972 Drop deformation and breakup in simple shear fields. PhD thesis, Chemical Engineering, Univ. of Houston, Texas.

TANGELDER, G. J., TEIRLINCK, H. C., SLAAF, D. W. & RENEMAN, R. S. 1985 Distribution of blood-platelets flowing in arterioles. *Am. J. Physiol.* **248** (3), H318–H323.

TRETHEWAY, D. C. & LEAL, L. G. 2001 Deformation and relaxation of Newtonian drops in planar extensional flows of a Boger fluid. *J. Non-Newtonian Fluid Mech.* **99**, 81–108.

TRYGGVASON, G., BUNNER, B., ESMAEELI, A., JURIC, D., AL-RAWAHI, N., TAUBER, W., HAN, J., NAS, S. & JAN, Y. J. 2001 A front-tracking method for the computations of multiphase flow. *J. Comput. Phys.* **169**, 708–759.

UIJTTEWAAL, W. S. J., NIJHOF, E. J. & HEETHAR, R. M. 1993 Droplet migration, deformation, and orientation in the presence of a plane wall: a numerical study compared with analytical theories. *Phys. Fluids* A **5**, 819–825.

YUE, P. T., FENG, J. J., LIU, C. & SHEN, J. 2005 Viscoelastic effects on drop deformation in steady shear. *J. Fluid Mech.* **540**, 427–437.